2020-06

Concept and performance of a novel wave energy converter: Variable Aperture Point-Absorber (VAPA)

Zheng, Siming

http://hdl.handle.net/10026.1/15352

10.1016/j.renene.2020.01.134
Renewable Energy
Elsevier BV

Title:

Concept and performance of a novel wave energy converter: Variable Aperture Point-Absorber (VAPA)

Author names and affiliations:
Siming Zheng[a,b], Yongliang Zhang[b], Gregorio Iglesias[c,a]

a *School of Engineering, Computing and Mathematics, University of Plymouth, Drake Circus, Plymouth PL4 8AA, UK*
b *State Key Laboratory of Hydroscience and Engineering, Tsinghua University, Beijing 100084, China*
c *School of Engineering & Environmental Research Institute, University College Cork, Cork, Ireland.*

Siming Zheng
siming.zheng@plymouth.ac.uk

Yongliang Zhang
yongliangzhang@tsinghua.edu.cn

Gregorio Iglesias
gregorio.iglesias@ucc.ie

Corresponding author:
Name: Prof Gregorio Iglesias
Tel: +441752586131
E-mail address: *gregorio.iglesias@ucc.ie*

Received 20 August 2018,
Revised 6 November 2019,
Accepted 27 January 2020,
Available online 30 January 2020.

DOI: 10.1016/j.renene.2020.01.134

Abstract: Ocean waves are a huge and largely untapped resource of green energy. In order to extract energy from waves, a novel wave energy converter (WEC) consisting of a floating, hollow cylinder capped by a roof with a variable aperture is presented in this paper. The power take-off (PTO) system is composed of a linear generator attached to the seabed, driven by the heave motion of the floating cylinder through a tether line. The air pressure within the cylinder can be modified by adjusting the roof aperture. The hydrodynamic characteristics of this WEC are investigated through an analytical model based on potential flow theory, in which the wave diffraction/radiation problems are coupled with the air pressure fluctuation and PTO system. Analytical expressions are derived for the maximum power absorbed by the WEC under different optimization principles, revolving around the PTO damping, roof aperture damping and non-negative mooring stiffness. We find that the best power absorption is obtained when the aperture is either completely open or entirely closed, depending on the wave conditions. Intermediate values of the aperture are useful to minimize the heave motion and thus ensure survivability under extreme sea states.

Keywords: Wave power; Wave energy converter; Marine renewable energy; Ocean energy; Point-absorber.

1. Introduction

Ocean waves constitute a vast energy resource (Iglesias and Carballo, 2009; Drew et al., 2009), and research to harness it is under way along a number of lines: the characterisation of the resource (e.g,, Carballo et al., 2014; Lopez et al., 2015); the combination of wave power with other renewables, notably offshore wind (e.g., Veigas and Iglesias, 2014; Astariz and Iglesias, 2016); the environmental impacts of wave farms (e.g., Veigas et al., 2014; Abanades et al., 2015); the economics of wave energy (e.g., Astariz and Iglesias, 2015; Contestabile et al., 2016); and, last but not least, the development of wave energy technology (e.g., Falcão, 2010; Babarit et al., 2012).

Point-absorbers are a particular type of WEC: floating devices smaller than the typical wave length and capturing wave power mainly through a translating motion relative to a reference point. Although not the most efficient WEC type, point-absorbers are advantageous considering total performance and energy costs (Sjolte et al., 2013a), their compact dimensions and simple construction (Chen et al., 2017).

Most of the point-absorbers developed so far are based on truncated cylinders, e.g., the Uppsala University heaving buoy (Figure 1), connected to a translator in a linear generator installed on the seabed (Hai et al., 2016). The translator has a limited stroke, and is equipped with springs to dampen endstop shocks. A peak force still occurs on the mooring line when the upper endstop spring is hit (Sjökvist and Göteman, 2017). The Ocean Power Technology PowerBuoy (Figure 2a) uses a damping plate for reference (Mekhiche and Edwards, 2014). Wavebob (Figure 2b) adopts a submerged float rather than a plate or the seabed for reference (Falcão, 2010). The submerged float allows the tuning to the incident wave frequency. Other point-absorbers (BOLT, CETO and Wavestar) are described in Ding et al. (2016), Ransley et al. (2017), and Ulvin et al. (2012).

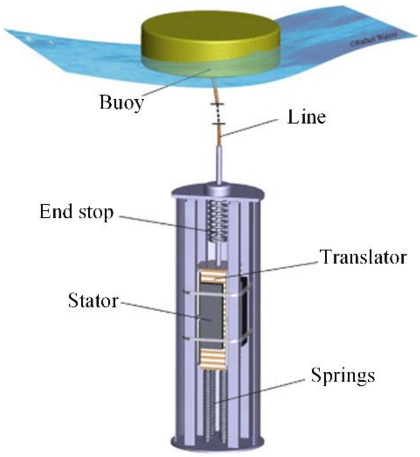

Fig. 1. Heaving buoy, Uppsala University (Falcão, 2010).

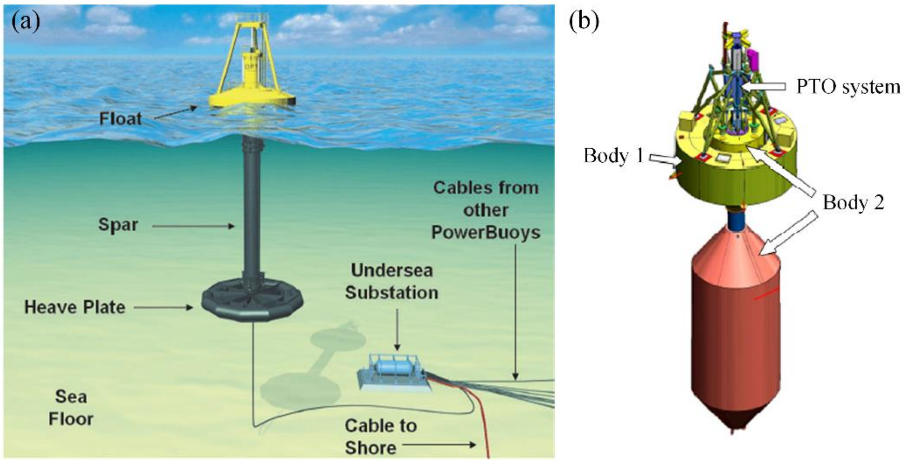

Fig. 2. (a) OPT PowerBuoy (Mekhiche and Edwards, 2014); (b) Wavebob (Falcão, 2010).

Chen et al. (2017); Engström et al. (2017); Gravråkmo (2014) and Göteman (2017) suggested that torus buoys (truncated cylinders with moonpools) may be advantageous for survivability given their reduced surge motion and line forces. Two examples are Lifesaver and Seabased (Fig.3). Lifesaver has three integrated PTOs (BOLT, 2018; Sjolte, 2014). Wave-to-wire simulations and array performance were reported by Sjolte et al. (2013a, 2013b). With Seabased, loadings on the upper endstop were smaller than for a truncated cylindrical buoy with the same water plane area and displacement, although 10.9% less power was delivered (Lejerskog et al., 2015). Thus, torus buoys have advantages for survivability, at the expense of slightly lower power absorption than conventional point-absorbers.

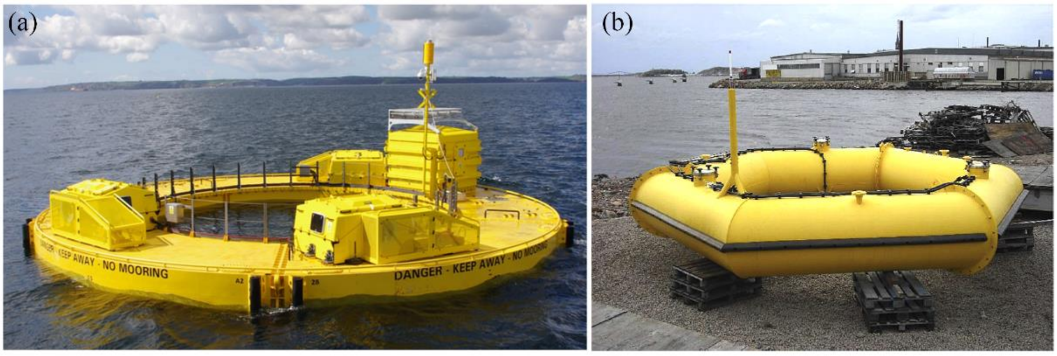

Fig. 3. (a) Lifesaver (Sjolte, 2014); (b) Seabased (Lejerskog et al., 2015).

The present work is motivated by three main objectives: to enhance the survivability of the system under extreme conditions, to reduce its cost, and to improve its wave power absorption in terms of the peak value of the frequency response. To this aim, a novel WEC, VAPA (Variable Aperture Point-Absorber), which combines the advantages of traditional point-absorbers (truncated cylinders) and torus buoys, is proposed and investigated. VAPA is a hollow cylinder with an inner chamber covered by a roof that can be opened totally or partially, and open at its bottom, below the waterline (Fig. 4). As the cylinder oscillates under wave action, so does the water column in the chamber, causing the air pressure in the chamber to fluctuate. Unlike floating oscillating water columns, there is no turbine installed on the roof. Instead, power extraction is achieved by a linear generator on the seabed, connected to the cylinder through a tether. The air pressure effect can be adjusted by changing the roof aperture. When the aperture is totally open, VAPA performs as a torus buoy, which is beneficial for survivability under extreme wave conditions; by contrast, when the aperture is totally closed, VAPA works like a traditional solid point-absorber with the water enclosed performing as ballast, which is beneficial in terms of cost (less weight of steel required) and wave power extraction (in particular, vis-à-vis the peak value of the frequency response). Thus, VAPA can switch between two configurations, the traditional point-absorber and the torus buoy, by changing the roof aperture, by means of an intelligent control system, the details of which are beyond the scope of the present article. To determine the effect of the roof aperture on power extraction, we develop, validate and apply an analytical model.

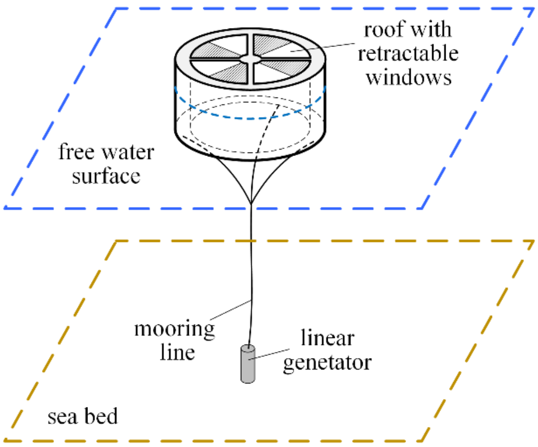

Fig. 4. VAPA schematic

2. Analytical model

For a preliminary performance assessment, the roof aperture effect is modelled as a linear damping, and nonlinear, viscous effects are neglected. Under an incident wave train of small amplitude, A, and angular frequency, ω, the free surface displacement in the chamber may be written as $Q=\mathrm{Re}\left(\hat{Q}\mathrm{e}^{-\mathrm{i}\omega t}\right)$, with $\hat{Q}$ the complex amplitude, t time, and i the imaginary unit. Air pressure in the chamber may be written as $p=\mathrm{Re}\left(\hat{p}\mathrm{e}^{-\mathrm{i}\omega t}\right)$, with $\hat{p}$ the complex amplitude. Assuming the mass flux across the roof aperture to be proportional to the pressure, and considering the effect of air compressibility, which results in a phase lag between Q and p, following Falcão and Sarmento (1980) and Sarmento and Falcão (1985) we have:

$$\hat{Q}=\left(c_{\mathrm{r}}-\frac{\mathrm{i}\omega V_0}{c_{\mathrm{a}}^2\rho_0}\right)\hat{p}, \tag{1}$$

where c_{r} is a damping coefficient representing the damping effect induced by the aperture on the roof. More specifically, it is related to the volume flux across the roof due to unit air pressure in the internal chamber. When $c_{\mathrm{r}}=0$, no volume flux will be excited regardless of the value of the internal air pressure, i.e., the roof aperture is totally closed; by contrast, when $c_{\mathrm{r}}=\infty$, volume flux can be very easily excited with a small value of internal air pressure, i.e., the roof aperture is totally open. V_0 is the air chamber volume, c_{a} denotes the sound velocity in air, and ρ_0 represents the static air density.

For small-amplitude regular waves, Q results from scattered (incident and diffracted) and radiated waves, which are induced both by cylinder oscillation and pressure oscillation. This also applies to the hydrodynamic forces acting on the float.

2.1 Governing equations and boundary conditions of wave diffraction and radiation problems

Let a vertical truncated circular cylinder of radius R with a moonpool of radius R_{i} float in water of finite depth h, with draught d. A Cartesian coordinate system is adopted, with the xy-plane at the mean water surface, the Ox-axis in the incident wave direction, and the Oz-axis along the cylinder axis, pointing upwards (Fig. 5). The cylinder has three DoFs: surge, heave and pitch. A local cylindrical coordinate system ($Or\theta$) is defined with r measuring radially from the z-axis and θ from the positive Ox-axis. The rotation center (r=0, z=z_0) may serve as the reference point to calculate the pitch wave excitation moment and hydrodynamic coefficients in relation with the oscillation in pitch mode.

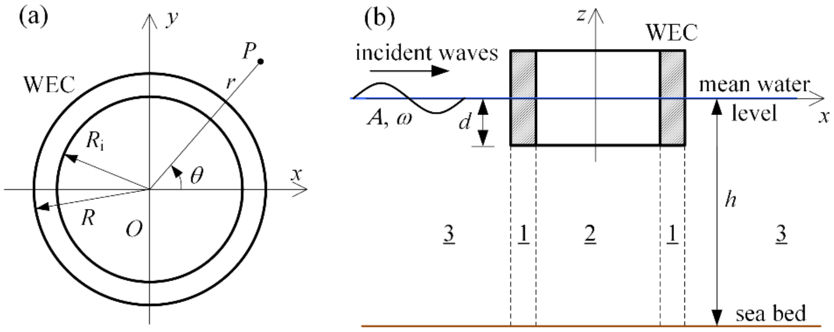

Fig. 5. Definition sketch: (a) Top view; (b) Side view.

Assuming the fluid to be isotropic, incompressible and inviscid, and the wave amplitude to be small, linear potential flow theory may be adopted to describe the hydrodynamic problem. The total spatial velocity potential $\varPhi$ may be decomposed into the incident, $\varPhi_{\mathrm{I}}$, diffracted, $\varPhi_{\mathrm{D}}$, and radiated wave spatial potential,

$$\varPhi = \varPhi_{\mathrm{I}} + \varPhi_{\mathrm{D}} + \sum_{j=1}^{3} \dot{A}_j \varPhi_{\mathrm{R}}^{(j)} + \hat{p}\varPhi_{\mathrm{R}}^{(0)}, \tag{2}$$

where $\dot{A}_j$ is the complex velocity amplitude of the chamber oscillating in j-th mode (with j=1,2,3 denoting surge, heave, and pitch, respectively); $\varPhi_{\mathrm{R}}^{(j)}$ is the spatial velocity potential due to a unit amplitude velocity oscillation in j-th mode; and $\varPhi_{\mathrm{R}}^{(0)}$ is the spatial velocity potential due to a unit air pressure oscillation.

The spatial velocity potential for the undisturbed incident regular waves propagating along the positive Ox axis may be written as

$$\varPhi_{\mathrm{I}} = -\frac{\mathrm{i}gA}{\omega}\frac{\cosh\left[k_0\left(z+h\right)\right]}{\cosh\left(k_0 h\right)}\mathrm{e}^{\mathrm{i}k_0 x}\text{, or as} \tag{3a}$$

$$\varPhi_{\mathrm{I}}\left(r,\theta,z\right) = -\frac{\mathrm{i}gA}{\omega}\frac{\cosh\left[k_0\left(z+h\right)\right]}{\cosh\left(k_0 h\right)}\sum_{m=-\infty}^{\infty}\mathrm{i}^m J_m\left(k_0 r\right)\mathrm{e}^{\mathrm{i}m\theta}, \tag{3b}$$

where Eq.(3a) employs the Cartesian coordinate system ($Oxyz$) and Eq.(3b) the local cylindrical coordinate systems ($Or\theta z$); k_0 is the wave number, which satisfies the dispersion relation, $\omega^2 = gk_0\tanh(k_0 h)$; and g is the gravitational acceleration.

The free-surface and body boundary conditions to be satisfied by $\varPhi_{\mathrm{D}}$ and $\varPhi_{\mathrm{R}}^{(j)}$ can be found in Mavrakos and Konispoliatis (2012), Zheng et al. (2018).

2.2 Spatial potentials in subdomains

The spatial potentials $\varPhi_{\mathrm{D}}$ and $\varPhi_{\mathrm{R}}^{(j)}$ (j=0,1,2,3) in fluid subdomain Region n can be written in a unified format as $\varPhi_n^{\chi}$, in which χ='D' and '(j)' represent the wave diffracted potential and the radiated potential due to air pressure oscillations inside the chamber (j=0) and cylinder motions in j-th mode (j=1,2,3), respectively. Applying the method of separation of variables in different regions, the general spatial potentials may be expressed by complex Fourier series as follows:

1) In Region 1

$$\varPhi_1^{\chi}\left(r,\theta,z\right) = \varPhi_{1,\mathrm{p}}^{\chi} + \sum_{m=-\infty}^{\infty}\left[\frac{E_{m,0}^{\chi}}{2} + \sum_{l=1}^{\infty}\left(A_{m,l}^{\chi}\frac{I_m\left(\beta_l r\right)}{I_m\left(\beta_l R\right)} + C_{m,l}^{\chi}\frac{K_m\left(\beta_l r\right)}{K_m\left(\beta_l R\right)}\right)\cos\left[\beta_l\left(z+h\right)\right]\right]\mathrm{e}^{\mathrm{i}m\theta} \tag{4}$$

where

$$E_{m,0}^{\chi} = \begin{cases} A_{m,0}^{\chi} + C_{m,0}^{\chi}\left[1+\ln\left(\dfrac{r}{R}\right)\right], & m=0 \\ A_{m,0}^{\chi}\left(\dfrac{r}{R}\right)^{|m|} + C_{m,0}^{\chi}\left(\dfrac{r}{R}\right)^{-|m|}, & m\neq 0 \end{cases} \tag{5}$$

I_m is the modified Bessel function of first kind and order m; K_m is the modified Bessel function of second kind and order m; $A_{m,l}^{\chi}$ and $C_{m,l}^{\chi}$ are unknown coefficients; β_l is the l-th eigenvalue:

$$\beta_l = \frac{l\pi}{h-d},\ l\text{=0, 1, 2, 3…}, \tag{6}$$

$\Phi_{1,\mathrm{p}}^{\chi}$ is a particular solution; for χ='D', $\Phi_{1,\mathrm{p}}^{\chi}$=-$\Phi_{\mathrm{I}}$; for χ='(j)' (j=0,1), $\Phi_{1,\mathrm{p}}^{\chi}$=0; and for χ='(j)' (j=2,3),

$$\Phi_{1,\mathrm{p}}^{(j)} = \begin{cases} \dfrac{1}{4(h-d)}\left[2(z+h)^2 - r^2\right], & j=2 \\ \dfrac{\cos\theta}{8(h-d)}\left[r^3 - 4r(z+h)^2\right], & j=3 \end{cases} \tag{7}$$

2) Region 2

$$\Phi_2^{\chi}(r,\theta,z) = \sum_{m=-\infty}^{\infty}\left[\frac{D_{m,0}^{\chi}J_m(k_0 r)Z_0(z)}{J_m(k_0 R_{\mathrm{i}})Z_0(0)} + \sum_{l=1}^{\infty}\frac{D_{m,l}^{\chi}I_m(k_l r)Z_l(z)}{I_m(k_l R_{\mathrm{i}})Z_l(0)}\right]\mathrm{e}^{\mathrm{i}m\theta} + \Phi_{2,\mathrm{p}}^{\chi} \tag{8}$$

where $D_{m,l}^{\chi}$ is the coefficient to be solved; J_m is the Bessel function of order m; k_l is the eigenvalue (Falnes, 2002).

$$\omega^2 = -gk_l\tan(k_l h),\quad l\text{=1, 2, 3, …} \tag{9}$$

$$Z_0(z) = N_0^{-0.5}\cosh\left[k_0(z+h)\right];\ Z_l(z) = N_l^{-0.5}\cos\left[k_l(z+h)\right]; \tag{10}$$

$$N_0 = \frac{1}{2}\left[1+\frac{\sinh(2k_0 h)}{2k_0 h}\right];\ N_l = \frac{1}{2}\left[1+\frac{\sin(2k_l h)}{2k_l h}\right]; \tag{11}$$

$\Phi_{2,\mathrm{p}}^{\chi}$ is a particular solution, which for χ='(0)', $\Phi_{2,\mathrm{p}}^{\chi} = -\mathrm{i}/(\rho\omega)$, ρ is the water density; whereas for χ='D' and '(j)'(j=1,2,3), $\Phi_{2,\mathrm{p}}^{\chi}$=0.

3) Region 3

The spatial potential in Region 3 represents the wave travelling outwards from the cylinder, and can be written as an eigen-function expansion,

$$\Phi_3^{\chi}(r,\theta,z) = \sum_{m=-\infty}^{\infty}\left[B_{m,0}^{\chi}\frac{H_m(k_0 r)}{H_m(k_0 R)}\frac{Z_0(z)}{Z_0(0)} + \sum_{l=1}^{\infty}B_{m,l}^{\chi}\frac{K_m(k_l r)}{K_m(k_l R)}\frac{Z_l(z)}{Z_l(0)}\right]\mathrm{e}^{\mathrm{i}m\theta}, \tag{12}$$

where H_m is the Hankel function of first kind of order m, and $B_{m,l}^{\chi}$ are unknown coefficients to be determined.

2.3 Method of computation for unknown coefficients

The expressions of the diffracted spatial potential and radiated potentials, Eqs. (4)~(12) in Section 2.2, should satisfy the conditions of continuity for pressure and normal velocity on the interfaces of the two adjacent subdomains, i.e., at $r=R$ and $r=R_\mathrm{i}$, as follows.:

1) Pressure at the boundary $r=R$:

$$\Phi_3^{\chi} = \Phi_1^{\chi}, \quad -h < z < -d, r = R \tag{13}$$

2) Pressure at the boundary $r=R_\mathrm{i}$:

$$\Phi_2^{\chi} = \Phi_1^{\chi}, \quad -h < z < -d, r = R_\mathrm{i} \tag{14}$$

3) Normal velocity at the boundary $r=R$:

For $-h < z < -d$,

$$\frac{\partial \Phi_3^{\chi}}{\partial r} = \frac{\partial \Phi_1^{\chi}}{\partial r}. \tag{15a}$$

For $-d < z < 0$,

$$\frac{\partial \Phi_3^{\chi}}{\partial r} = \begin{cases} -\dfrac{\partial \Phi_1}{\partial r}, & \chi = \text{'D'} \\ \delta_{1,j}\cos\theta + \delta_{3,j}\left(z - z_0\right)\cos\theta, & \chi = \text{'}(j)\text{'} \end{cases}, \tag{15b}$$

in which δ is the Kronecker delta function.

4) Normal velocity at the boundary $r=R_\mathrm{i}$:

For $-h < z < -d$

$$\frac{\partial \Phi_2^{\chi}}{\partial r} = \frac{\partial \Phi_1^{\chi}}{\partial r}. \tag{16a}$$

For $-d < z < 0$

$$\frac{\partial \Phi_2^{\chi}}{\partial r} = \begin{cases} -\dfrac{\partial \Phi_1}{\partial r}, & \chi = \text{'D'} \\ \delta_{1,j}\cos\theta + \delta_{3,j}\left(z - z_0\right)\cos\theta, & \chi = \text{'}(j) \end{cases}. \tag{16b}$$

Upon substituting the diffracted and radiated spatial potentials, Eqs. (4)~(12), into Eqs. (13)~(16), utilizing the orthogonal properties of the functions cos($n\theta$), sin($n\theta$), and Z_l(z), and rearranging, the diffracted and radiated spatial potentials in each subdomain can be obtained by solving a matrix equation, in which the infinite series are truncated by choosing ($2M$+1) terms (m=–M, …, 0, …, M) for $e^{im\theta}$ functions and L_0+1 terms (l=0, 1, 2, … L_0) for Z_l(z) and cos[β_l(z+h)] functions (Zheng and Zhang, 2015, 2016, 2018).

2.4 Wave excitation volume flux/forces

The rate of free surface displacement inside the chamber due to the contributions of the undisturbed incident wave and the diffracted wave can be written as $\mathrm{Re}\left[F_{\mathrm{e}}^{(0)}\mathrm{e}^{-\mathrm{i}\omega t}\right]$, where, with utilization of Eq. (3) and Eq. (8),

$$\begin{aligned} F_{\mathrm{e}}^{(0)} &= \int_0^{2\pi}\int_0^{R_{\mathrm{i}}} \left.\frac{\partial\left(\Phi_{\mathrm{I}}+\Phi_{\mathrm{D}}\right)}{\partial z}\right|_{z=0} r\mathrm{d}r\mathrm{d}\theta = \frac{\omega^2}{g}\int_0^{2\pi}\int_0^{R_{\mathrm{i}}} \left.\left(\Phi_{\mathrm{I}}+\Phi_2^{\mathrm{D}}\right)\right|_{z=0} r\mathrm{d}r\mathrm{d}\theta \\ &= \frac{2\pi\omega^2 R_{\mathrm{i}}}{g}\left[-\frac{\mathrm{i}gA}{\omega}\frac{J_1\left(k_0R_{\mathrm{i}}\right)}{k_0} + \frac{D_{0,0}^{\mathrm{D}}J_1\left(k_0R_{\mathrm{i}}\right)}{k_0J_0\left(k_0R_{\mathrm{i}}\right)} + \sum_{l=1}^{\infty}\frac{D_{0,l}^{\mathrm{D}}I_1\left(k_lR_{\mathrm{i}}\right)}{k_lI_0\left(k_lR_{\mathrm{i}}\right)}\right] \end{aligned} \quad (17)$$

The wave excitation forces due to the incident wave acting on structures which are stationary can be computed from the incident wave potential and the diffracted potential. The generalized wave excitation force on the WEC chamber in j-th mode (j=1,2,3) is $\mathrm{Re}\left[F_{\mathrm{e}}^{(j)}\mathrm{e}^{-\mathrm{i}\omega t}\right]$, where

$$F_{\mathrm{e}}^{(j)} = -\mathrm{i}\omega\rho\int_S\left(\Phi_{\mathrm{I}}+\Phi_{\mathrm{D}}\right)n_j\mathrm{d}s\,. \quad (18)$$

in which $n_1=n_x$, $n_2=n_z$, $n_3=(z-z_0)n_x-xn_z$, $\vec{n}=n_x\vec{i}+n_y\vec{j}+n_z\vec{k}$ is the unit normal vector directed into the fluid domain at the wetted surface of the cylinder.

2.5 Hydrodynamic coefficients

An upward flux at the water surface inside the chamber (radiation volume flux) and forces on the floats (radiation forces) can be induced when the air pressure inside the chamber or the cylinder oscillate in the absence of an incident wave.

The complex amplitudes of the radiation volume flux due to a unit amplitude velocity oscillation of the WEC chamber oscillating in j-th mode (j=1,2,3) and a unit air pressure oscillation inside the WEC (j=0) can be written, respectively, as:

$$\begin{aligned} F_{\mathrm{R},j}^{(0)} &= \int_0^{2\pi}\int_0^{R_{\mathrm{i}}} \left.\frac{\partial\Phi_2^{(j)}}{\partial z}\right|_{z=0} r\mathrm{d}r\mathrm{d}\theta = \frac{\omega^2}{g}\int_0^{2\pi}\int_0^{R_{\mathrm{i}}}\Phi_2^{(j)} r\mathrm{d}r\mathrm{d}\theta \\ &= \frac{2\pi\omega^2 R_{\mathrm{i}}}{g}\left[\frac{D_{0,0}^{(j)}J_1\left(k_0R_{\mathrm{i}}\right)}{k_0J_0\left(k_0R_{\mathrm{i}}\right)} + \sum_{l=1}^{\infty}\frac{D_{0,l}^{(j)}I_1\left(k_lR_{\mathrm{i}}\right)}{k_lI_0\left(k_lR_{\mathrm{i}}\right)}\right] = \mathrm{i}\omega a_{0,j} - c_{0,j} \end{aligned} \quad (19)$$

where $a_{0,j}$ and $c_{0,j}$ are called the hydrodynamic coefficients.

Similarly, the complex amplitudes of radiation force exerted on the WEC chamber in j'-th mode (j'=1,2,3) due to unit amplitude velocity oscillation of the chamber oscillating in j-th mode and unit air pressure oscillation inside the WEC (j=0) can be respectively written in terms of the hydrodynamic coefficients $a_{j',j}$ and $c_{j',j}$ as:

$$F_{\mathrm{R},j}^{(j')} = -\mathrm{i}\omega\rho\int_S\Phi_{\mathrm{R}}^{(j)}n_{j'}\mathrm{d}s = \mathrm{i}\omega a_{j',j} - c_{j',j}\,. \quad (20)$$

The method for calculating the hydrodynamic coefficients as given in Eqs. (19)-(20) is straightforward based on the definitions of radiation volume flux and radiation forces. Hence it is referred henceforth as the “direct method (DM)”. In fact, there is a Haskind relation (HR) between wave diffraction and radiation problems (Falnes, 2002), and a number of hydrodynamic coefficients can be written in terms of the wave excitation volume flux and wave excitation forces as:

$$c_{j,j} = \frac{k_0}{4\rho g v_{\mathrm{g}} A^2}\left|F_{\mathrm{e}}^{(j)}\right|^2, \ (j\text{=0, 2}) \tag{21}$$

$$c_{j',j} = \frac{k_0}{8\rho g v_{\mathrm{g}} A^2} F_{\mathrm{e}}^{(j')} F_{\mathrm{e}}^{(j)*}, \ (j\text{=1, 3; } j'\text{=1, 3}) \tag{22}$$

$$a_{j,j'} = \frac{k_0 \mathrm{i}}{4\omega\rho g v_{\mathrm{g}} A^2} F_{\mathrm{e}}^{(j)} F_{\mathrm{e}}^{(j')*}, \ ((j, j')\text{=(0, 2) and (2, 0)}) \tag{23}$$

where ‘*’ denotes the complex-conjugate, and v_{g} is the wave group velocity expressed as

$$v_{\mathrm{g}} = \frac{\omega}{2k_0}\left[1 + \frac{2k_0 h}{\sinh(2k_0 h)}\right]. \tag{24}$$

2.6 Response and power absorption of the VAPA WEC

For the novel WEC under regular waves of small amplitude, after coupling the chamber oscillation with the air pressure fluctuation and PTO system, the matrix equation of motion in the frequency domain may be written as

$$\left[-\mathrm{i}\omega\left(\mathbf{M}_{\mathrm{a}} + \mathbf{M}_{\mathrm{PTO}} + \mathbf{M}\right) + \left(\mathbf{C}_{\mathrm{d}} + \mathbf{C}_{\mathrm{PTO}} + \mathbf{C}_{\mathrm{r}}\right) + \mathrm{i}\left(\mathbf{K}_{\mathrm{s}} + \mathbf{K}_{\mathrm{m}}\right)/\omega\right]\dot{\boldsymbol{X}} = \boldsymbol{F}_{\mathrm{e}}, \tag{25}$$

where $\dot{\boldsymbol{X}}$ is the motion/pressure response vector written as $\dot{\boldsymbol{X}} = \left[\hat{p}, \dot{A}_1, \dot{A}_2, \dot{A}_3\right]^{\mathrm{T}}$, in which the motion response of the floats are given in terms of velocities, ‘T’ denotes the transpose; $\boldsymbol{F}_{\mathbf{e}}$ represents the wave excitation volume flux/force acting on the device, and it is a 4×1 vector, written as $\boldsymbol{F}_{\mathrm{e}} = \left[F_{\mathrm{e}}^{(0)}, F_{\mathrm{e}}^{(1)}, F_{\mathrm{e}}^{(2)}, F_{\mathrm{e}}^{(3)}\right]^{\mathrm{T}}$. $\mathbf{M_a}$ and $\mathbf{C_d}$ are two 4×4 square matrices of added-mass and radiation damping coefficients due to wave radiation, which can be calculated, together with $\boldsymbol{F}_{\mathrm{e}}$, from Sections 2.4 and 2.5. $\mathbf{M_{PTO}}$ is a diagonal matrix of mass coefficients of Power Take-Off system (PTO) in the device, the diagonal elements of which can be written as $1/\left(c_{\mathrm{a}}^2\rho_0\right)[V_0, 0, 0, 0]^{\mathrm{T}}$. Here, $V_0 = \pi R_1^2 d$ is adopted with c_{a}=340 m/s and ρ/ρ_0=1000, following Martins-rivas and Mei (2009). The non-vanishing elements involved in $\mathbf{M_{PTO}}$ are used to consider the effect of compressibility of air in the chamber. $\mathbf{C_{PTO}}$ represents a diagonal matrix of the damping coefficients of the PTO written as $diag(\mathbf{C}_{\mathrm{PTO}}) = [0, 0, c_{\mathrm{PTO}}, 0]^{\mathrm{T}}$, in which c_{PTO} represents the PTO damping induced by the linear generator connected to the WEC; $\mathbf{C}_{\mathrm{r}}$ is a matrix used to consider the damping effect induced by the aperture size of the roof, the volume flux created by the heaving motion of the WEC chamber, and the force on the horizontal roof of the WEC due to its inner pressure. These effects are reflected by the non-vanishing elements, c_r, πR_i^2 and $-\pi R_i^2$, located at the first row and the first column, the first row and the third column, and the third row and the first column of $\mathbf{C}_r$, respectively. $\mathbf{M}$ and $\mathbf{K}_s$ are the mass matrix and hydrostatic stiffness matrix of the device. For the effect of hydrostatic stiffness on the air pressure enclosed by the chamber has already been included in radiation coefficients (Falnes, 2002), different from those for traditional floats, no separate term is required in $\mathbf{K}_s$ for the air pressure. We assume the WEC is half submerged at equilibrium with the mass uniformly distributed all over its chamber body. $\mathbf{K}_m$ is the restoring stiffness matrix induced by the mooring lines. Here we consider mainly the spring effect on the heave motions, which is the most prominent influence of the mooring system, and disregard other effects, such as damping or inertia. Thus, there is only one non-vanishing element, located on the diagonal line as: $diag(\mathbf{K}_m)=[0,0,k_m,0]^T$, where k_m is the moorings restoring force coefficient in heave mode of the WEC. Actually, the stiffness in the PTO system can also be treated as a part of k_m.

In regular waves, the time-averaged absorbed power of the novel WEC can be expressed as:

$$P = \frac{1}{2} c_{\mathrm{PTO}} \left| \dot{A}_2 \right|^2. \tag{26}$$

The capture factor, also called the relative capture width, can be defined by

$$\eta = \frac{P}{2RP_{\mathrm{in}}}, \tag{27}$$

where P_{in} represents the incoming wave power per unit width of the wave front (Zheng and Zhang, 2018).

2.7 Maximization of power absorption

Although the system has four degrees of freedom, Eq. (25), the surge motion (and also the pitch motion) are decoupled from the heave motion and the internal air pressure; therefore, the advantage of the hollow cylinder in terms of survivability thanks to its weaker surge motion still applies to the VAPA WEC. The heave motion used to capture wave power is only coupled with the air pressure enclosed by the WEC chamber. Therefore, a two DOF motion matrix equation as given below can be used also to evaluate the heave motion of VAPA:

$$\begin{bmatrix} S_{1,1}+c_{\mathrm{r}} & S_{1,2} \\ S_{2,1} & c_{\mathrm{PTO}}+\mathrm{i}\,k_{\mathrm{m}}/\omega+S_{2,2} \end{bmatrix} \begin{Bmatrix} \hat{p} \\ \dot{A}_2 \end{Bmatrix} = \begin{Bmatrix} F_{\mathrm{e}}^{(0)} \\ F_{\mathrm{e}}^{(2)} \end{Bmatrix}, \tag{28}$$

where

$$S_{1,1} = c_{0,0} - \mathrm{i}\omega\left(a_{0,0} + \frac{V_0}{c_a^2 \rho_0} \right);\ S_{1,2} = c_{0,2} + \pi R_{\mathrm{i}}^2 - \mathrm{i}\omega a_{0,2};\ S_{2,1} = c_{2,0} - \pi R_{\mathrm{i}}^2 - \mathrm{i}\omega a_{2,0};$$

$$S_{2,2} = c_{2,2} - \mathrm{i}\omega\left(a_{2,2} + m_0 - \frac{\rho g s_0}{\omega^2} \right), \tag{29}$$

in which s_0 denotes the cross-sectional area of the device.

The expression of the heave velocity can be derived as:

$$\dot{A}_2 = \frac{F_{\mathrm{e}}^{(2)} - F_{\mathrm{e}}^{(0)} S_{2,1} \big/ \left(S_{1,1} + c_{\mathrm{r}}\right)}{c_{\mathrm{PTO}} + \mathrm{i}\, k_{\mathrm{m}} / \omega + S_{2,2} - S_{2,1} S_{1,2} \big/ \left(S_{1,1} + c_{\mathrm{r}}\right)}, \tag{30}$$

The power absorbed in the PTO damping is:

$$P = \frac{\left(c_{\mathrm{PTO}}/2\right) \left| F_{\mathrm{e}}^{(2)} - F_{\mathrm{e}}^{(0)} S_{2,1} \big/ \left(S_{1,1} + c_{\mathrm{r}}\right) \right|^2}{\left| c_{\mathrm{PTO}} + \mathrm{i}\, k_{\mathrm{m}} / \omega + S_{2,2} - S_{2,1} S_{1,2} \big/ \left(S_{1,1} + c_{\mathrm{r}}\right) \right|^2}. \tag{31}$$

There are three variables involved in the expression of P, i.e., c_{PTO}, k_{m} and c_{r}. The more variables that are optimized at the same time, the more complicated the design/control system that is required, with the consequent difficulties for practical applications. Therefore, in addition to the optimization of two or three variables at the same time, the optimization of individual variables is considered in the following.

1) Optimization of the PTO damping coefficient

We note that P=0 for c_{PTO} =0 and for c_{PTO} =∞, and that P> 0 for $0 < c_{\mathrm{PTO}} < \infty$. Thus there is a maximum of absorbed power when $\partial P/\partial c_{\mathrm{PTO}} = 0$, which occurs if:

$$c_{\mathrm{PTO}} = \sqrt{\kappa_1^2 + \left(\kappa_2 + k_{\mathrm{m}}/\omega\right)^2} \equiv c_{\mathrm{opt}}^{(\mathrm{PTO})}, \tag{32}$$

where κ_1 and κ_2 are two real parameters introduced from

$$\kappa_1 + \mathrm{i}\kappa_2 = S_{2,2} - S_{2,1} S_{1,2} \big/ \left(S_{1,1} + c_{\mathrm{r}}\right), \tag{33}$$

in which κ_1 is found and can also be proved positive regardless of the WEC scales (see Eq. (A1) in Appendix A). Note that both κ_1 and κ_2 are dependent of c_{r}. Therefore, referring to Eq. (32), the optimal c_{PTO} for maximizing power absorption, i.e. $c_{\mathrm{opt}}^{(\mathrm{PTO})}$, is influenced by both c_{r} and k_{m}.

The corresponding maximum of absorbed power is

$$P_{\max}^{(\mathrm{PTO})} = \frac{\left| F_{\mathrm{e}}^{(2)} - F_{\mathrm{e}}^{(0)} S_{2,1} \big/ \left(S_{1,1} + c_{\mathrm{r}}\right) \right|^2 \big/ 4}{\kappa_1 + \sqrt{\kappa_1^2 + \left(\kappa_2 + k_{\mathrm{m}}/\omega\right)^2}}. \tag{34}$$

2) Optimization of the mooring stiffness

With reference to Eq. (31), if only k_{m} is variable, the maximum power absorption occurs when $k_{\mathrm{m}}/\omega+\kappa_2=0$, i.e.,

$$k_{\mathrm{m}} = -\omega\kappa_2 \equiv k_{\mathrm{opt}}^{(\mathrm{m})}, \tag{35}$$

which is only affected by c_r, regardless of c_{PTO}.

The corresponding maximum of absorbed power is

$$P_{max}^{(m)} = \frac{\left|F_e^{(2)} - F_e^{(0)} S_{2,1} / \left(S_{1,1} + c_r\right)\right|^2 c_{PTO}}{2\left|c_{PTO} + \kappa_1\right|^2}. \tag{36}$$

In practice, k_m should be non-negative, hence Eqs. (35) and (36) are rewritten as:

$$k_{opt}^{(m)} = \begin{cases} -\omega\kappa_2, & \kappa_2 \le 0 \\ 0, & \kappa_2 > 0 \end{cases}, \tag{37}$$

$$P_{max}^{(m)} = \begin{cases} \dfrac{\left|F_e^{(2)} - F_e^{(0)} S_{2,1} / \left(S_{1,1} + c_r\right)\right|^2 c_{PTO}}{2\left|c_{PTO} + \kappa_1\right|^2}, & \kappa_2 \le 0 \\ \dfrac{\left|F_e^{(2)} - F_e^{(0)} S_{2,1} / \left(S_{1,1} + c_r\right)\right|^2 c_{PTO}}{2\left|c_{PTO} + \kappa_1 + \mathrm{i}\kappa_2\right|^2}, & \kappa_2 > 0 \end{cases}. \tag{38}$$

3) Optimization of the roof damping coefficient

The analysis the effect of c_r on the power absorption is obviously more complicated than those for the optimization of c_{PTO} and k_m. After making some rearrangement, the power absorbed by the novel WEC as expressed in Eq. (31) can be rewritten as:

$$P = \frac{\left(c_{PTO}/2\right)\left|F_e^{(2)}\right|^2 \left|c_r + S_{1,1} - F_e^{(0)} S_{2,1} / F_e^{(2)}\right|^2}{\left|c_{PTO} + \mathrm{i}\,k_m/\omega + S_{2,2}\right|^2 \left|c_r + S_{1,1} - S_{2,1}S_{1,2} / \left(c_{PTO} + \mathrm{i}\,k_m/\omega + S_{2,2}\right)\right|^2}. \tag{39}$$

There can be two different solutions of c_r satisfying $\partial P/\partial c_r=0$. It is found through analytical experiments that only one of the two roots is positive, which is written as:

$$c_r = \frac{\xi_1^2 + \xi_2^2 - \xi_3^2 - \xi_4^2 + \sqrt{\left(\xi_1^2 + \xi_2^2 - \xi_3^2 - \xi_4^2\right)^2 - 4\left(\xi_3 - \xi_1\right)\left[\xi_1\left(\xi_3^2 + \xi_4^2\right) - \xi_3\left(\xi_1^2 + \xi_2^2\right)\right]}}{2\left(\xi_3 - \xi_1\right)}, \tag{40}$$

where ξ_1, ξ_2, ξ_3 and ξ_4 are four real parameters introduced from

$$\xi_1 + \mathrm{i}\xi_2 = S_{1,1} - F_e^{(0)} S_{2,1} / F_e^{(2)}\,;\ \xi_3 + \mathrm{i}\xi_4 = S_{1,1} - S_{2,1}S_{1,2} / \left(c_{PTO} + \mathrm{i}\,k_m/\omega + S_{2,2}\right). \tag{41}$$

According to Haskind relation, it can be known from Eqs.(21)~(23) that

$$F_e^{(0)} / F_e^{(2)} = -\mathrm{i}\sqrt{c_{0,0}/c_{2,2}}\,sign\left(a_{02}\right);\ \omega a_{02} = \sqrt{c_{0,0}c_{2,2}}\,sign\left(a_{02}\right), \tag{42}$$

using which we have $\xi_1 \equiv 0$; $\xi_3 > 0$ is also satisfied regardless of c_{PTO} and k_m which can be proved in Eq.(A2), as given in Appendix A.

Since $\xi_3 > 0$, the value of c_r calculated from Eq. (40) minimizes power absorption rather than maximizes it. Hence the c_r obtained from Eq. (40) can be denoted as $c_{r,min}$. This is reasonable for the roof aperture exerts a linear damping, implying power dissipation, which results in diminished power absorption by the WEC. Therefore, $c_{r,min}$ may be seen as the optimal option for reducing the heave oscillation of the WEC, i.e., for survivability under extreme wave conditions. The corresponding minimum absorbed power $P_{\mathrm{min}}^{(\mathrm{r})}$ may be easily evaluated by substituting Eq. (40) into Eq. (39).

The maximum power absorption can be evaluated after making a comparison between the results with c_r=0 and ∞; its analytical expression is:

$$P_{\mathrm{max}}^{(\mathrm{r})}=\begin{cases}\dfrac{(c_{\mathrm{PTO}}/2)\left|F_{\mathrm{e}}^{(2)}\right|^2}{\left|c_{\mathrm{PTO}}+\mathrm{i}\,k_{\mathrm{m}}/\omega+S_{2,2}\right|^2}, & \dfrac{\xi_1^2+\xi_2^2}{\xi_3^2+\xi_4^2}\le 1\\ \dfrac{(c_{\mathrm{PTO}}/2)\left|F_{\mathrm{e}}^{(2)}-F_{\mathrm{e}}^{(0)}S_{2,1}/S_{1,1}\right|^2}{\left|c_{\mathrm{PTO}}+\mathrm{i}\,k_{\mathrm{m}}/\omega+S_{2,2}-S_{2,1}S_{1,2}/S_{1,1}\right|^2}, & \dfrac{\xi_1^2+\xi_2^2}{\xi_3^2+\xi_4^2}>1\end{cases}, \tag{43}$$

for which the corresponding optimal c_r is

$$c_{\mathrm{opt}}^{(\mathrm{r})}=\begin{cases}\infty, & \dfrac{\xi_1^2+\xi_2^2}{\xi_3^2+\xi_4^2}\le 1\\ 0, & \dfrac{\xi_1^2+\xi_2^2}{\xi_3^2+\xi_4^2}>1\end{cases}, \tag{44}$$

implying that to improve power capture width of the novel WEC, the roof should either be entirely open, or be completely closed.

4) Optimization of the PTO damping coefficient and the roof damping coefficient

The expressions of these optimal values of c_{PTO}, k_m and c_r as derived above are obtained when each of them is regarded as the only variable parameter. Furthermore, when both c_{PTO} and c_r can be arbitrarily specified, the maximum power could be:

$$P_{\mathrm{max}}^{(\mathrm{PTO,r})}=\max\{p_1,p_2\}, \tag{45}$$

where

$$p_1=\frac{\left|F_{\mathrm{e}}^{(2)}\right|^2/4}{c_{2,2}+\sqrt{c_{2,2}^2+\left[\omega\left(a_{2,2}+m_0\right)-\left(\rho g s_0+k_{\mathrm{m}}\right)/\omega\right]^2}}, \tag{46}$$

$$p_2=\frac{\left|F_{\mathrm{e}}^{(2)}-F_{\mathrm{e}}^{(0)}S_{2,1}/S_{1,1}\right|^2/4}{\zeta_1+\sqrt{\zeta_1^2+\left(\zeta_2+k_{\mathrm{m}}/\omega\right)^2}}, \tag{47}$$

in which ζ_1 and ζ_2 are two real parameters satisfying

$$\zeta_1 + \mathrm{i}\zeta_2 = S_{2,2} - S_{2,1}S_{1,2}/S_{1,1} \,. \tag{48}$$

The corresponding optimal values of c_{PTO} and c_{r} are written as:

$$\left\{c_{\mathrm{opt,PTO}}^{(\mathrm{PTO,r})},\quad c_{\mathrm{opt,r}}^{(\mathrm{PTO,r})}\right\} = \begin{cases} \left\{\sqrt{c_{2,2}^2 + \left[\omega\left(a_{2,2}+m_0\right) - \left(\rho g s_0 + k_{\mathrm{m}}\right)/\omega\right]^2},\quad \infty\right\}, & P_{\max}^{(\mathrm{PTO,r})} = p_1 \\ \left\{\sqrt{\zeta_1^2 + \left(\zeta_2 + k_{\mathrm{m}}/\omega\right)^2},\quad 0\right\}, & P_{\max}^{(\mathrm{PTO,r})} = p_2 \end{cases} . \tag{49}$$

Note: ζ_1 can be treated as an special root of κ_1 with c_{r} =0, thus we have ζ_1>0 as well.

5) Optimization of the PTO damping coefficient and the mooring stiffness

It can be seen by inspection of Eqs. (32)~(34) that if c_{PTO} and k_{m} can be chosen such that

$$\begin{cases} c_{\mathrm{PTO}} = \kappa_1 \equiv c_{\mathrm{opt}}^{(\mathrm{PTO,m})} \\ k_{\mathrm{m}} = -\omega\kappa_2 \equiv k_{\mathrm{opt}}^{(\mathrm{PTO,m})} \end{cases}, \tag{50}$$

then the maximum absorbed power is

$$P_{\max}^{(\mathrm{PTO,m})} = \frac{\left|F_{\mathrm{e}}^{(2)} - F_{\mathrm{e}}^{(0)} S_{2,1}/\left(S_{1,1}+c_{\mathrm{r}}\right)\right|^2}{8\kappa_1} . \tag{51}$$

Considering k_{m} to be non-negative, the maximum absorbed power and the corresponding optimized c_{PTO} and k_{m} can be rewritten as

$$P_{\max}^{(\mathrm{PTO,m})} = \begin{cases} \dfrac{\left|F_{\mathrm{e}}^{(2)} - F_{\mathrm{e}}^{(0)} S_{2,1}/\left(S_{1,1}+c_{\mathrm{r}}\right)\right|^2}{8\kappa_1}, & \kappa_2 \le 0 \\ P_{\max}^{(\mathrm{PTO})}(k_{\mathrm{m}}=0), & \kappa_2 > 0 \end{cases} . \tag{52}$$

$$\left\{c_{\mathrm{opt}}^{(\mathrm{PTO,m})},\quad k_{\mathrm{opt}}^{(\mathrm{PTO,m})}\right\} = \begin{cases} \left\{\kappa_1,\quad -\omega\kappa_2\right\}, & \kappa_2 \le 0 \\ \left\{c_{\mathrm{opt}}^{(\mathrm{PTO})}\left(k_{\mathrm{m}}=0\right),\quad 0\right\}, & \kappa_2 > 0 \end{cases} . \tag{53}$$

6) Optimization of the roof damping coefficient and the mooring stiffness

Similar to the optimization of c_{PTO} and c_{r}, when both c_{r} and k_{m} can be arbitrarily specified the maximum absorbed power is

$$P_{\max}^{(\mathrm{r,m})} = \max\left\{p_1', p_2'\right\}, \tag{54}$$

in which

$$p_1' = \frac{\left(c_{\mathrm{PTO}}/2\right)\left|F_{\mathrm{e}}^{(2)}\right|^2}{\left(c_{\mathrm{PTO}}+c_{2,2}\right)^2}, \quad p_2' = \frac{\left(c_{\mathrm{PTO}}/2\right)\left|F_{\mathrm{e}}^{(2)}-F_{\mathrm{e}}^{(0)}S_{2,1}/S_{1,1}\right|^2}{\left(c_{\mathrm{PTO}}+\zeta_1\right)^2}. \tag{55}$$

The corresponding optimal c_{r} and k_{m} are written as

$$\left\{c_{\mathrm{opt}}^{(\mathrm{r,m})},\quad k_{\mathrm{opt}}^{(\mathrm{r,m})}\right\} = \begin{cases} \left\{\infty,\quad \omega^2\left(a_{2,2}+m_0\right)-\rho g s_0\right\}, & P_{\max}^{(\mathrm{r,m})} = p_1' \\ \left\{0,\quad -\omega\zeta_2\right\}, & P_{\max}^{(\mathrm{r,m})} = p_2' \end{cases}. \tag{56}$$

With consideration of the non-negative property of k_{m}, Eqs. (54) and (56) can be rewritten as

$$P_{\max}^{(\mathrm{r,m})} = \max\left\{p_1' f\left[\omega^2\left(a_{2,2}+m_0\right)-\rho g s_0\right],\quad p_2' f\left(-\omega\zeta_2\right),\quad P_{\max}^{(\mathrm{r})}\left(k_{\mathrm{m}}=0\right)\right\}, \tag{57}$$

where

$$f\left(x\right) = \begin{cases} 1, & x \ge 0 \\ 0, & x < 0 \end{cases}, \tag{58}$$

and

$$\left\{c_{\mathrm{opt}}^{(\mathrm{r,m})},\quad k_{\mathrm{opt}}^{(\mathrm{r,m})}\right\} = \begin{cases} \left\{\infty,\quad \omega^2\left(a_{2,2}+m_0\right)-\rho g s_0\right\}, & P_{\max}^{(\mathrm{r,m})} = p_1' \\ \left\{0,\quad -\omega\zeta_2\right\}, & P_{\max}^{(\mathrm{r,m})} = p_2' \\ \left\{c_{\mathrm{opt}}^{(\mathrm{r})}\left(k_{\mathrm{m}}=0\right),\quad 0\right\}, & P_{\max}^{(\mathrm{r,m})} = P_{\max}^{(\mathrm{r})}\left(k_{\mathrm{m}}=0\right) \end{cases}. \tag{59}$$

7) Optimization of the PTO damping coefficient, the roof damping coefficient and the mooring stiffness

Furthermore, referring to Eq. (54), if c_{PTO} is also included as a variable parameter in the optimization, i.e., if c_{PTO}, c_{r} and k_{m} are optimized concurrently, the maximum absorbed power can be written as:

$$P_{\max}^{(\mathrm{PTO,r,m})} = \max\left\{P_1, P_2\right\}, \tag{60}$$

where

$$P_1 = \frac{\left|F_{\mathrm{e}}^{(2)}\right|^2}{8c_{2,2}}; \quad P_2 = \frac{\left|F_{\mathrm{e}}^{(2)}-F_{\mathrm{e}}^{(0)}S_{2,1}/S_{1,1}\right|^2}{8\zeta_1}, \tag{61}$$

in which P_1 represents the maximum absorbed power by the WEC with its roof completely open; whereas P_2 denotes the one when the roof is entirely closed. In fact, it can be proved that $P_2 \equiv P_1$, as given in Eq. (A3) in Appendix A. Hence Eq.(60) simplifies to:

$$P_{\max}^{(\mathrm{PTO,r,m})} = \frac{\left|F_{\mathrm{e}}^{(2)}\right|^2}{8c_{2,2}}. \tag{62}$$

The corresponding optimal c_{PTO}, c_{r} and k_{m} have two solutions, wrtten as

$$\left\{c_{\text{opt,PTO}}^{(\text{PTO,r,m})},\quad c_{\text{opt,r}}^{(\text{PTO,r,m})},\quad k_{\text{opt}}^{(\text{PTO,r,m})}\right\}=\begin{cases}\left\{c_{2,2},\quad \infty,\quad \omega^2\left(a_{2,2}+m_0\right)-\rho g s_0\right\}\\ \left\{\zeta_1,\quad 0,\quad -\omega\zeta_2\right\}\end{cases}. \tag{63}$$

The capture factors corresponding to $P_{\max}^{(\cdots)}$ can be denoted as $\eta_{\max}^{(\cdots)}$, in which from Eqs. (21), (27) and (62), we have

$$\eta_{\max}^{(\text{PTO,r,m})}=\frac{1}{2k_0R}. \tag{64}$$

Actually, with heave motion as the only mode of oscillation for any single axisymmetric body, it has been first derived independently by Budal and Falnes (1975); Evans (1976); Newman (1976) that the maximum absorption width (defined as the ratio between P and P_{in}) is equal to $1/k_0$. The results of Eq.(64) reveals that when c_{PTO}, c_{r} and k_{m} can be optimized at the same time, the theoretical maximum absorbed power and wave capture factor of the novel WEC are all the same to those of a solid cylinder with the same radius, regardless of compressibility of the air in the chamber.

If we consider the mooring stiffness non-negative, we have:

$$P_{\max}^{(\text{PTO,r,m})}=\max\left\{\frac{\left|F_{\text{e}}^{(2)}\right|^2}{8c_{2,2}}f\left[\omega^2\left(a_{2,2}+m_0\right)-\rho g s_0\right],\quad \frac{\left|F_{\text{e}}^{(2)}\right|^2}{8c_{2,2}}f\left(-\omega\zeta_2\right),\quad P_{\max}^{(\text{PTO,r})}\left(k_{\text{m}}=0\right)\right\}. \tag{65}$$

$$\left\{c_{\text{opt,PTO}}^{(\text{PTO,r,m})},\quad c_{\text{opt,r}}^{(\text{PTO,r,m})},\quad k_{\text{opt}}^{(\text{PTO,r,m})}\right\}=\begin{cases}\left\{c_{2,2},\quad \infty,\quad \omega^2\left(a_{2,2}+m_0\right)-\rho g s_0\right\}, & \left[\omega^2\left(a_{2,2}+m_0\right)-\rho g s_0\right]\geq 0\\ \left\{\zeta_1,\quad 0,\quad -\omega\zeta_2\right\}, & -\omega\zeta_2\geq 0\\ \left\{c_{\text{opt,PTO}}^{(\text{PTO,r})}\left(k_{\text{m}}=0\right),\quad c_{\text{opt,r}}^{(\text{PTO,r})}\left(k_{\text{m}}=0\right),\quad 0\right\}, & P_{\max}^{(\text{PTO,r,m})}=P_{\max}^{(\text{PTO,r})}\left(k_{\text{m}}=0\right)\end{cases}. \tag{66}$$

3. Validation of the analytical model

The dimensionless quantities of the non-vanishing wave excitation volume flux/forces and hydrodynamic coefficients are defined by:

$$\bar{F}_{\text{e}}^{(0)}=\frac{F_{\text{e}}^{(0)}}{\omega\pi R_{\text{i}}^2A};\ \bar{F}_{\text{e}}^{(j)}=\frac{F_{\text{e}}^{(j)}}{\rho g\pi\left(R^2-R_{\text{i}}^2\right)d^iA},\ (j=1,2,3) \tag{67}$$

where i=0 for j =1,2; whereas i=1 for j=3.

$$\bar{a}_{0,0}=\frac{\omega^2\rho a_{0,0}}{R_{\text{i}}};\ \bar{c}_{0,0}=\frac{\omega\rho c_{0,0}}{R_{\text{i}}}, \tag{68a}$$

$$\bar{a}_{j',j}=\frac{a_{j',j}}{\rho\pi\left(R^2-R_{\rm i}^2\right)d^i};\ \bar{c}_{j',j}=\frac{c_{j',j}}{\omega\rho\pi\left(R^2-R_{\rm i}^2\right)d^i},\ (j,j'=1,2,3) \tag{68b}$$

where i=1 for (j, j')=(1, 1) and (2, 2); i=2 for (j, j')=(1, 3) and (3, 1); whereas i=3 for (j, j')=(3, 3),

$$\bar{a}_{j',j}=\frac{\omega a_{j',j}}{\pi\left(R^2-R_{\rm i}^2\right)};\ \bar{c}_{j',j}=\frac{c_{j',j}}{\pi\left(R^2-R_{\rm i}^2\right)},\ (j,j')=(0,2)\text{ or }(2,0). \tag{68c}$$

The PTO damping induced by the linear generator ($c_{\rm PTO}$), the damping induced by the size of the aperture on the roof ($c_{\rm r}$), and the moorings restoring force coefficient ($k_{\rm m}$) are normalized as:

$$\bar{c}_{\rm PTO}=\frac{c_{\rm PTO}\sqrt{gh}}{\rho g d\left(R^2-R_{\rm i}^2\right)},\ \bar{c}_{\rm r}=\frac{c_{\rm r}\rho\sqrt{g/h}}{R_{\rm i}},\ \bar{k}_{\rm m}=\frac{k_{\rm m}}{\rho g\left(R^2-R_{\rm i}^2\right)} \tag{69}$$

The dimensionless quantities of the optimal PTO damping and the moorings restoring force coefficient corresponding to $P_{\rm max}^{(\cdots)}$ are denoted as $\bar{c}_{\rm opt,PTO}^{(\cdots)}$, $\bar{c}_{\rm opt,r}^{(\cdots)}$ and $\bar{k}_{\rm opt,m}^{(\cdots)}$, respectively, which can be obtained from $c_{\rm opt,PTO}^{(\cdots)}$, $c_{\rm opt,r}^{(\cdots)}$ and $k_{\rm opt,m}^{(\cdots)}$ following the same normalizing principles in Eq. (69).

In our analytical computations for all the cases below, we take M=20, L_0=50 to obtain converged results using the eigen-series analysis described above. To keep things simple, the wave number k_0 is represented by k in the following sections.

3.1 Wave diffraction and radiation

Nader (2013) applied a three-dimensional FEM (Finite Element Method) model to a heaving cylindrical OWC with the following dimensionless parameters: R/h=0.25, $R_{\rm i}/h$=0.2, d/h=0.2. The FEM model is based on linear potential flow theory and the discretisation of the entire computational water domain into a finite number of elements, where the quantity of interest is approximated. Neither the wave excitation forces nor the hydrodynamic coefficients related to the surge or pitch modes were considered in this FEM model. The corresponding coefficients can be evaluated with commercial codes based on the conventional BEM (Boundary Element Method), such as WAMIT and ANSYS-AQWA. In this section, the present analytical model is applied to study wave diffraction and radiation from the VAPA WEC with the same basic dimensionless parameters used by Nader (2013). For validation the analytical results are compared with numerical results from both FEM (Nader, 2013) and ANSYS-AQWA (ANSYS AQWA, 2011) codes.

Figure 6 presents the results of wave excitation forces and volume flux using different methods. It is apparent that the analytical results agree well with those from other methods.

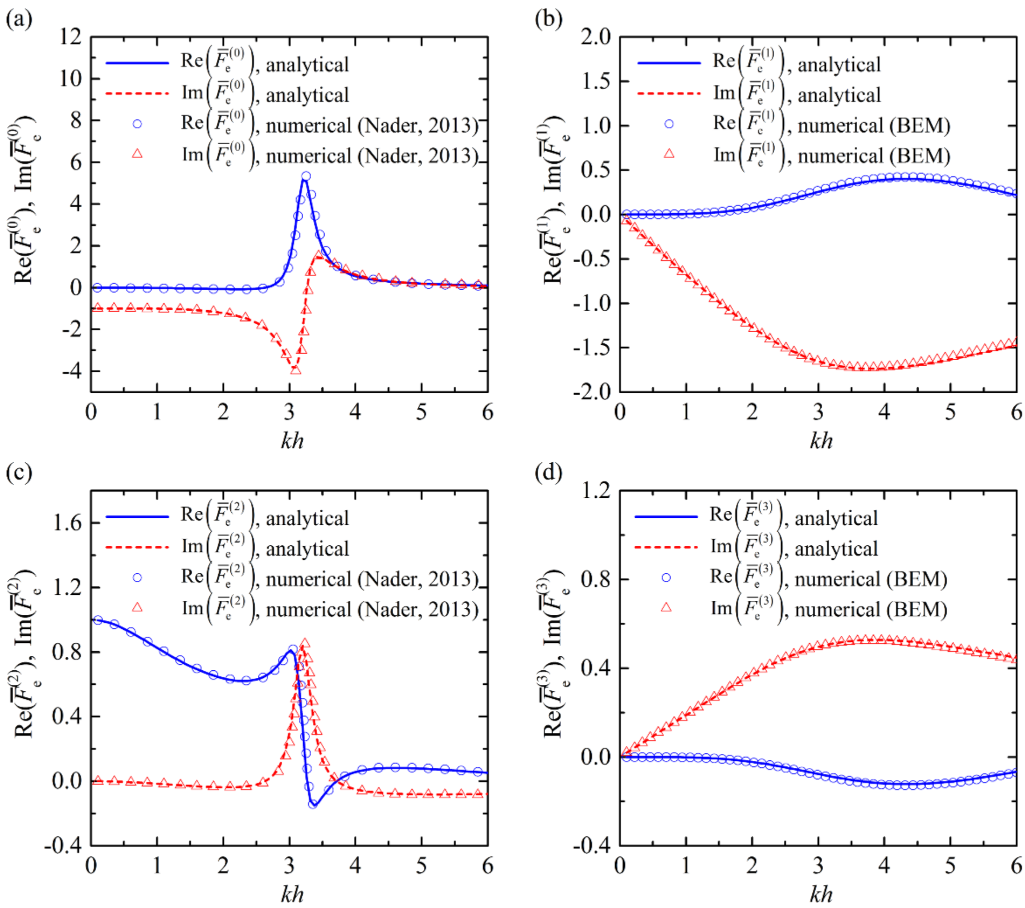

Fig. 6. Real and imaginary parts of the dimensionless wave excitation volume flux and forces against *kh*, (a) wave excitation volume flux; (b) surge wave excitation force; (c) heave wave excitation force; (d) pitch wave excitation moment.

Note that the case studied in this paper is a circular truncated cylinder with a circular moonpool; therefore, in addition to the plane y=0, x=0 is also a plane of symmetry. It follows that n_1 and n_3 in Eq. (20) are odd functions of x, whereas $\Phi_R^{(0)}$ and $\Phi_R^{(2)}$ are even functions. Hence $F_{R,0}^{(1)} = F_{R,0}^{(3)} = F_{R,2}^{(1)} = F_{R,2}^{(3)}$ =0. Moreover, the reciprocity relations $F_{R,j}^{(j')} = F_{R,j'}^{(j)}$ and $F_{R,j}^{(j')} = -F_{R,j'}^{(j)}$ are satisfied for (j=1,2,3; j'=1,2,3) and (j=1,2,3; j'=0 or j=0; j'=1,2,3), respectively, for the wave radiation problem of the present case (Falnes, 2002). Therefore, the only nonvanishing off-diagonal elements of the radiation hydrodynamic matrix are $F_{R,3}^{(1)} = F_{R,1}^{(3)}$ and $F_{R,0}^{(2)} = -F_{R,2}^{(0)}$. The normalised hydrodynamic coefficients corresponding to the nonvanishing $F_{R,j}^{(j')}$ in the frequency domain as a function of *kh* are plotted in Fig. 7.

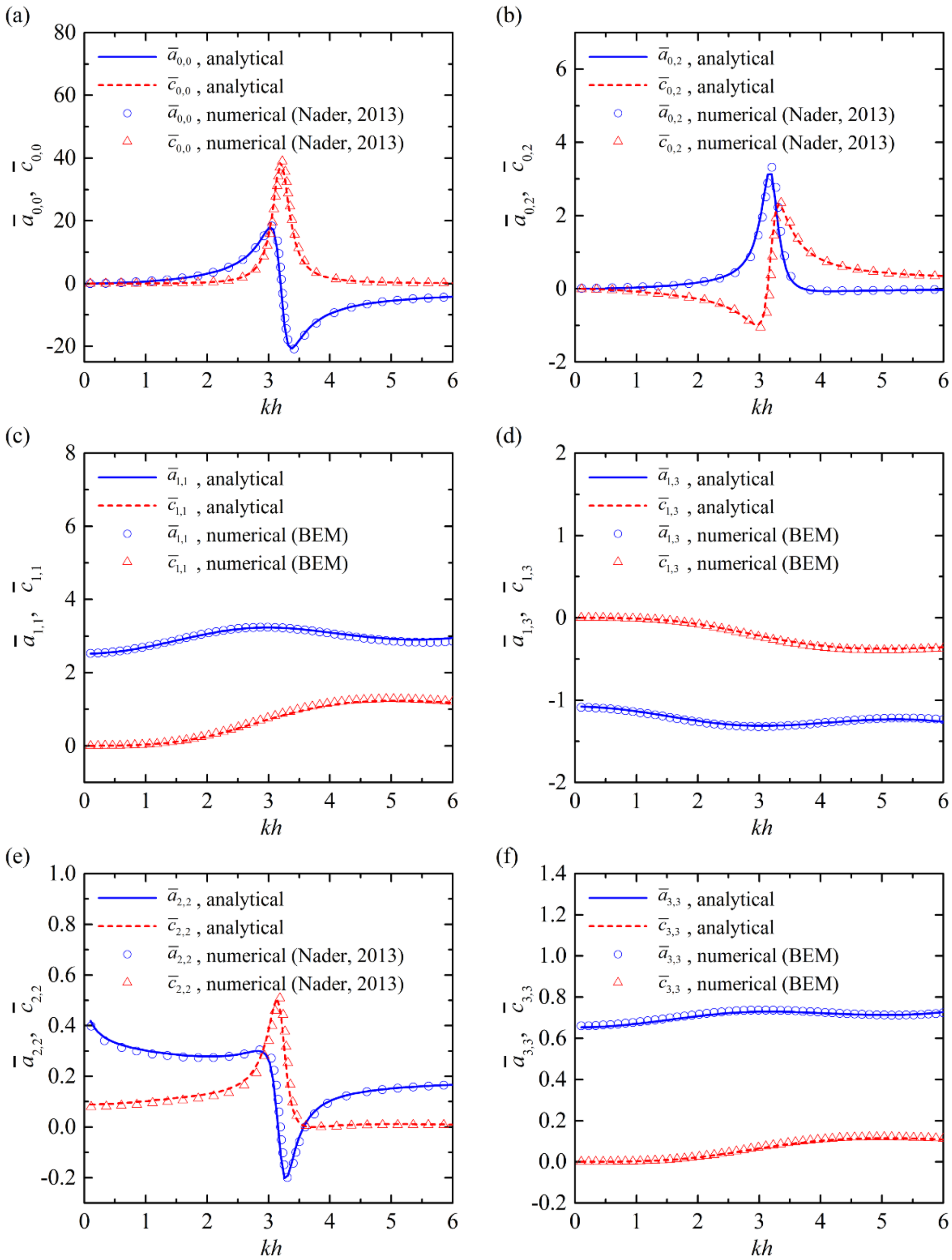

Fig. 7. Dimensionless hydrodynamic coefficients against *kh*, (a) $\bar{a}_{0,0}$ and $\bar{c}_{0,0}$; (b) $\bar{a}_{0,2}$ and $\bar{c}_{0,2}$; (c) $\bar{a}_{1,1}$ and $\bar{c}_{1,1}$; (d) $\bar{a}_{1,3}$ and $\bar{c}_{1,3}$; (e) $\bar{a}_{2,2}$ and $\bar{c}_{2,2}$; (f) $\bar{a}_{3,3}$ and $\bar{c}_{3,3}$.

Additionally, the hydrodynamic coefficients calculated by means of the DM and Haskind relation are listed and compared in Table 1. It may be seen that our results satisfy the Haskind relation between the diffraction and radiation problems very well, further proving the capability of the analytical model to solve the hydrodynamic problem of the novel WEC.

Table 1 Comparison of the hydrodynamic coefficients using DM and the Haskind relation

kh		1.0	2.0	3.0	4.0	5.0	6.0
$\overline{c}_{0,0}$	DM	0.01970	0.39500	15.18591	1.74723	0.34245	0.12341
	HR	0.01970	0.39499	15.18521	1.74711	0.34242	0.12339
$\overline{a}_{0,2}$	DM	0.03373	0.17064	1.81294	-0.06358	-0.04666	-0.02572
	HR	0.03373	0.17064	1.81294	-0.06358	-0.04666	-0.02572
$\overline{c}_{1,1}$	DM	0.03446	0.25872	0.72426	1.11079	1.23236	1.17622
	HR	0.03446	0.25872	0.72426	1.11079	1.23236	1.17622
$\overline{c}_{1,3}$	DM	-0.00957	-0.07553	-0.21734	-0.33762	-0.37581	-0.35729
	HR	-0.00957	-0.07553	-0.21733	-0.33762	-0.37581	-0.35728
$\overline{c}_{2,2}$	DM	0.10207	0.13028	0.38249	0.00409	0.01123	0.00948
	HR	0.10207	0.13028	0.38249	0.00409	0.01123	0.00948
$\overline{c}_{3,3}$	DM	0.00266	0.02205	0.06522	0.10262	0.11460	0.10853
	HR	0.00266	0.02205	0.06522	0.10262	0.11460	0.10852

3.2 Maximization of power absorption

In this section, we consider the case of a VAPA with dimensionless parameters: R/h=0.15, R_i/h=0.1, and d/h=0.1, as an example to validate the power absorption optimization by means of the analytical model.

Figure 8 presents the variation of $\eta_{\max}^{(\mathrm{PTO})}$ and $\overline{c}_{\mathrm{opt}}^{(\mathrm{PTO})}$ vs. kh for $\overline{k}_{\mathrm{m}}$=0, $\overline{c}_{\mathrm{r}}$=1 obtained with the present analytical model and by trial and error. The trial and error ("brute force") method may be described as an exhaustive search approach characterized by repeated, varied attempts until success without any intelligent algorithms employed. In Figures 9 and 10 these two methods, the present model and trial and error, are employed to evaluate the maximum and minimum power absorption of the device when only c_{r} can be varied. Figure 11 presents the results when both c_{r} and k_{m} can be optimized.

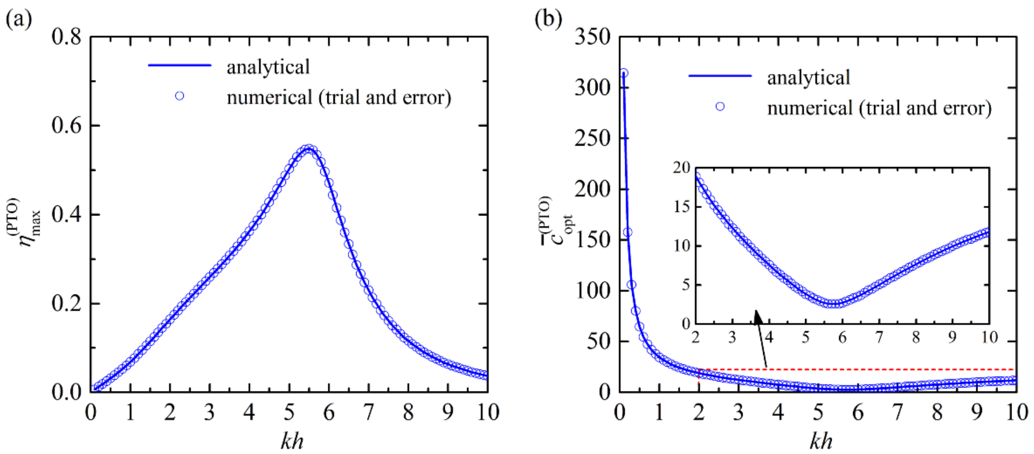

Fig. 8. Variation of $\eta_{\max}^{(\mathrm{PTO})}$ and $\overline{c}_{\mathrm{opt}}^{(\mathrm{PTO})}$ with kh for $\overline{k}_{\mathrm{m}}$=0, $\overline{c}_{\mathrm{r}}$=1.

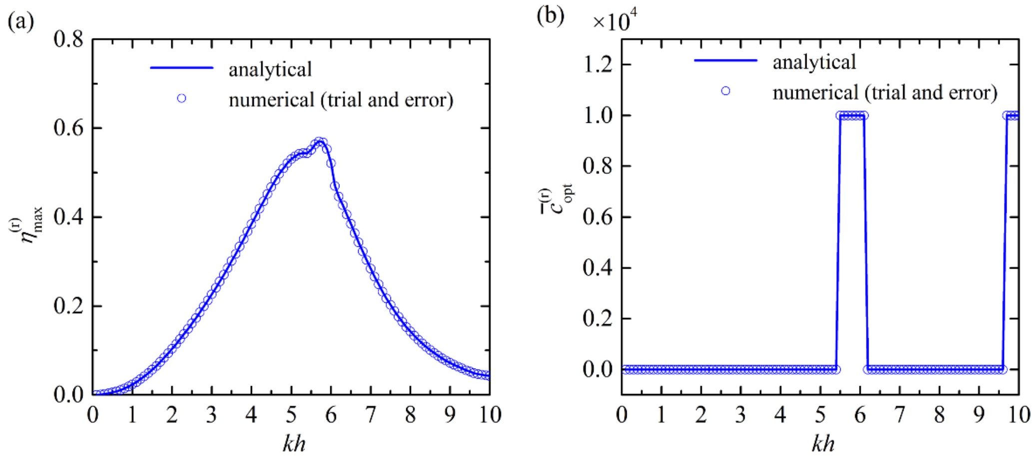

Fig. 9. Variation of $\eta_{\max}^{(\mathrm{r})}$ and $\bar{c}_{\mathrm{opt}}^{(\mathrm{r})}$ with kh for $\bar{k}_{\mathrm{m}}$ =0, $\bar{c}_{\mathrm{PTO}}$ =5.

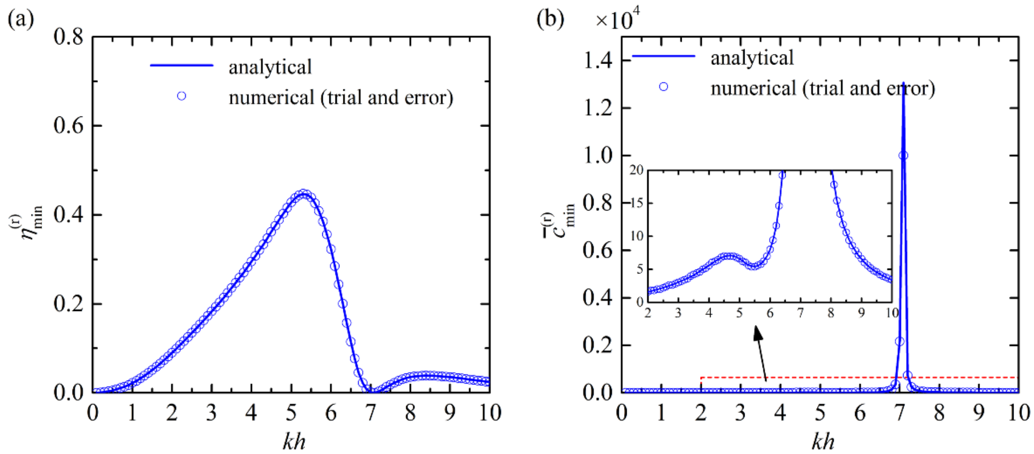

Fig. 10. Variation of $\eta_{\min}^{(\mathrm{r})}$ and $\bar{c}_{\min}^{(\mathrm{r})}$ with kh for $\bar{k}_{\mathrm{m}}$ =0, $\bar{c}_{\mathrm{PTO}}$ =5.

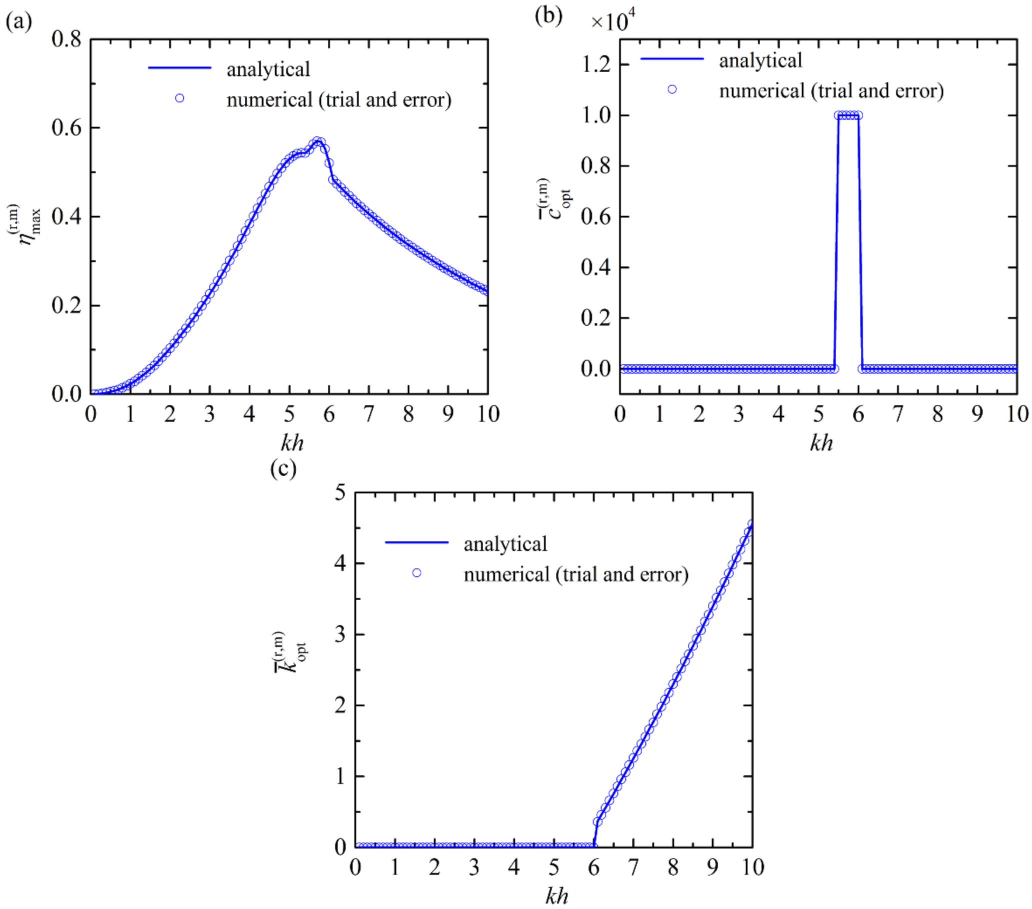

Fig. 11. Variation of $\eta_{\max}^{(\mathrm{r,m})}$, $\bar{c}_{\mathrm{opt}}^{(\mathrm{r,m})}$ and $\bar{k}_{\mathrm{opt}}^{(\mathrm{r,m})}$ with kh for $\bar{c}_{\mathrm{PTO}}$=5.

As shown in Figs. 8~11, there is excellent agreement between the analytical and numerical optimization results, corroborating the correctness of the expressions derived in Section 2.7.

4. Results and discussion

In this section the validated analytical model is employed to investigate the power extraction by a VAPA WEC with the following dimensionless parameters: R/h=0.15, R_i/h=0.1, d/h=0.1. After solving the wave diffraction and radiation problems, the excitation forces and volume flux, and the hydrodynamic coefficients with respect to the oscillating water column and the heave motion of the chamber are presented in Figure 12. As shown in Fig.12a, $\left|\bar{F}_{\mathrm{e}}^{(0)}\right|$ and $\left|\bar{F}_{\mathrm{e}}^{(2)}\right|$ reach their peak values of 6.44 and 0.97, respectively, at kh = 6.2 and 6.1. We have $\left|\bar{F}_{\mathrm{e}}^{(2)}\right|$ = 0 at kh = 7.1. In Fig.12b, $\bar{a}_{0,0}$ = 0 occurs at kh = 6.2, which corresponds to the resonant wave frequency of the device as a fixed OWC. In Fig.12c, apart from $\bar{a}_{2,2}$ and $\bar{c}_{2,2}$, a combination parameter $\left(\rho g s_0/\omega^2 - m_0\right)/\left[\rho\pi\left(R^2 - R_i^2\right)d\right]$ versus kh is also plotted into a black dot curve. An intersection point of such curve and the blue solid curve (i.e., $\bar{a}_{2,2}$-kh) is observed at kh=8.3, which is the resonant wave frequency of the device when it works with the roof entirely open. Since $\bar{a}_{2,0}$ and $\bar{c}_{2,0}$ are exactly the oppsite of $\bar{a}_{0,2}$ and $\bar{c}_{0,2}$, here Fig.12d only presents variation of the latter two hydrodynamic coefficients with kh.

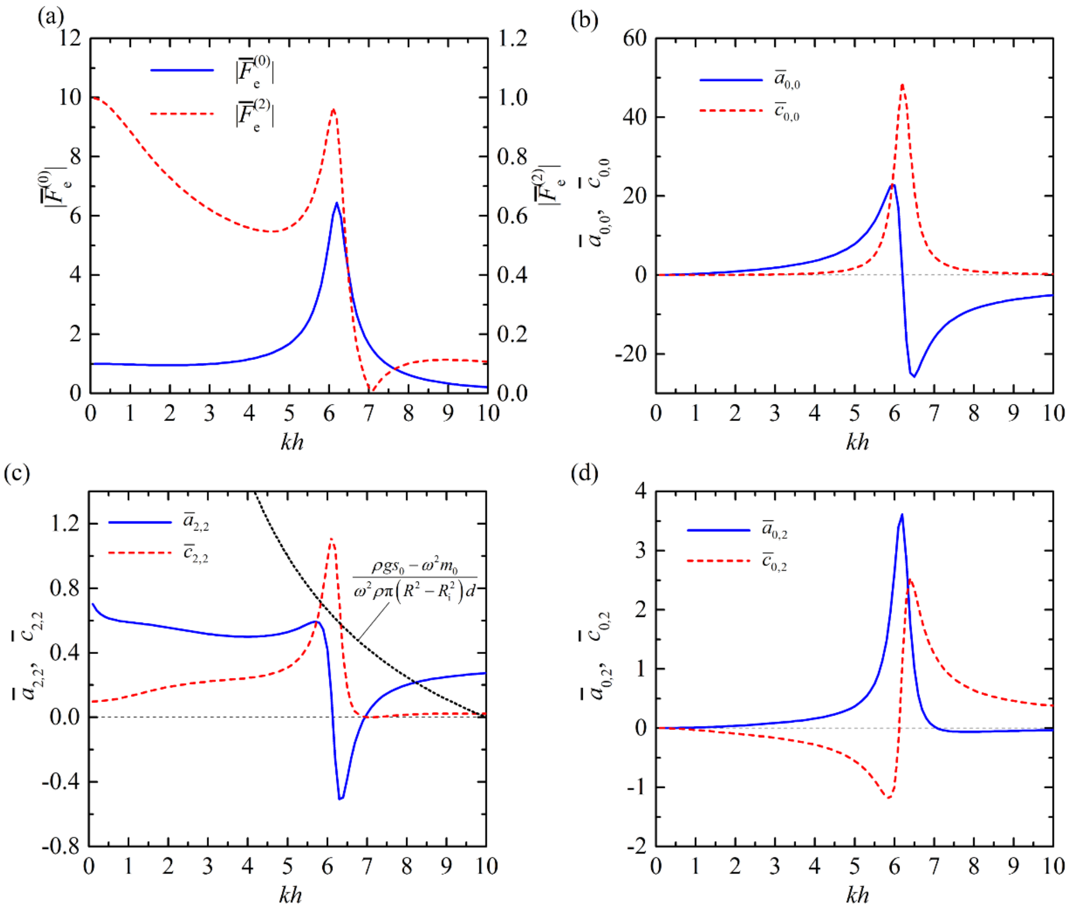

Fig. 12. Dimensionless wave excitation force/volume flux and hydrodynamic coefficients regarding oscillating water column and heave motion of the chamber against kh for R/h=0.15, R_i/h=0.1, d/h=0.1: (a) $\left|\bar{F}_e^{(0)}\right|$ and $\left|\bar{F}_e^{(2)}\right|$; (b) $\bar{a}_{0,0}$ and $\bar{c}_{0,0}$; (c) $\bar{a}_{2,2}$ and $\bar{c}_{2,2}$; (d) $\bar{a}_{0,2}$ and $\bar{c}_{0,2}$.

The power absorption of the novel WEC can be evaluated by combining the solutions of the diffraction/radiation problems with power take-off systems by means of Eq. (25). Figure 13 presents variation of η with kh for different $\bar{c}_r$, i.e., different aperture size of the roof, and $\bar{k}_m$=0, $\bar{c}_{PTO}$=5. As indicated, changing the size of the roof aperture leads to obvious changes in the frequency response of η. With the aperture entirely closed the device captures more power than with the aperture completely open for most wave conditions, except in the range $5.5 < kh < 6.1$. As $\bar{c}_r$ increases from 0 towards ∞, the kh corresponding to the peak of η-kh curve increases, whereas the peak value of η first decreases and then increases after reaching a minimum value. Among the six cases with different values of $\bar{c}_{\mathrm{r}}$ as plotted in Fig. 13, the minimum peak value of η is 0.46 occurring at kh=5.4 with $\bar{c}_{\mathrm{r}}$=10, while the maximum peak value of η is 0.57 occurring at kh=5.7 with $\bar{c}_{\mathrm{r}}=\infty$, which is 1.24 times as large as the minimum one. In addition to the curves for the novel WEC, the power absorption of a conventional (solid cylinder) point-absorber with the same scales of R and d is plotted as well. It is found that the novel WEC with the roof entirely closed works almost all the same in absorbing power with traditional point-absorber using solid cylinder. Since the surge motion is decoupled from the heave motion, surge is not affected by the size of the roof aperture, i.e., the surge motion of the novel WEC is independent of the aperture size, and is the same as that of a hollow cylinder without a roof. This means that a hollow cylinder with the roof aperture completely closed performs similarly to a solid cylinder in capturing wave power; however, since the displacement of the hollow cylinder is much smaller than that of the solid cylinder, from a cost point of view, the novel WEC could be more attractive than traditional point-absorber. Additionally, compared with the solid cylinder, the hollow cylinder might be advantageous in terms of survivability as well because it presents less motion in surge mode, as reported by Engström et al. (2017); Gravråkmo (2014) and Göteman (2017).

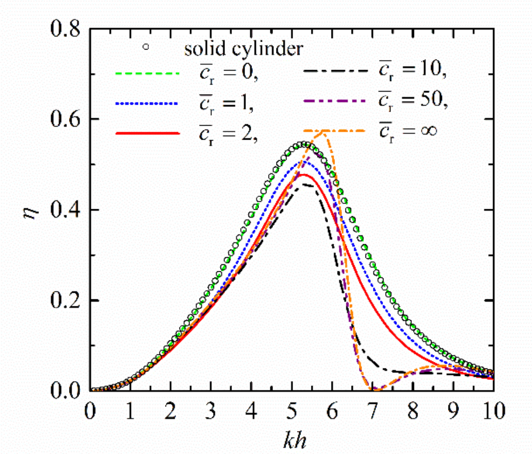

Fig. 13. Variation of η with kh for different $\bar{c}_{\mathrm{r}}$ and $\bar{k}_{\mathrm{m}}$=0, $\bar{c}_{\mathrm{PTO}}$=5.

The results as shown in Fig. 13 are those without optimization of any parameters. The maximum power extraction of the device with different optimization principles as derived in Section 2.7 is presented and discussed in the following sections.

4.1 Optimization of the PTO damping coefficient

Figure 14 illustrates the variation of the maximum power capture factor of the novel WEC ($\eta_{\max}^{(\mathrm{PTO})}$) and the corresponding optimal PTO damping coefficient ($\bar{c}_{\mathrm{opt}}^{(\mathrm{PTO})}$) with wave number ($kh$) for $\bar{k}_{\mathrm{m}}$=0. Different curves represent the device with different values of c_{r}. When the aperture size of the roof is small, e.g., $\bar{c}_{\mathrm{r}}$ <10, $\eta_{\max}^{(\mathrm{PTO})}$-*kh* presents the characteristics of a unimodal curve with $\eta_{\max}^{(\mathrm{PTO})}$ peaking at *kh*=5.5. For such cases, the $\bar{c}_{\mathrm{opt}}^{(\mathrm{PTO})}$ -*kh* performs as a single-valley-curve, and $\bar{c}_{\mathrm{opt}}^{(\mathrm{PTO})}$ reaches the minimum value at *kh*=5.7, slightly different from that where the peak of $\eta_{\max}^{(\mathrm{PTO})}$ occurs. For $\bar{c}_{\mathrm{r}}$ <10, the larger the aperture size is, the smaller both $\eta_{\max}^{(\mathrm{PTO})}$ and $\bar{c}_{\mathrm{opt}}^{(\mathrm{PTO})}$ are for most wave conditions, except 5.0<*kh*<7.0, where $\bar{c}_{\mathrm{opt}}^{(\mathrm{PTO})}$ is nearly independent of $\bar{c}_{\mathrm{r}}$. As the roof aperture size turns larger and larger ($\bar{c}_{\mathrm{r}}$ ≥10), frequency response of $\eta_{\max}^{(\mathrm{PTO})}$ changes towards a bimodal curve, in which the second peak appears at *kh*=8.3 where resonance occurs. Meanwhile, a vanishing power absorption point is also obtained at *kh*=7.1. This is due to no wave excitation force acting on the chamber (see Fig.12a) and very limited interacting air/hydrodynamic force exerted on the roof/chamber bottom because of the negligible air pressure. Although the peaks of $\left|\bar{F}_{\mathrm{e}}^{(0)}\right|$ and $\left|\bar{F}_{\mathrm{e}}^{(2)}\right|$ both occur at *kh*=6.1~6.2, the main peak of $\eta_{\max}^{(\mathrm{PTO})}$-*kh* is found at a rather smaller *kh*, i.e., 5.5~5.7. This can be explained from Fig.12c, which indicates a large difference between $\bar{a}_{2,2}$ and $\left(\rho g s_0/\omega^2 - m_0\right)/\left[\rho\pi\left(R^2-R_{\mathrm{i}}^2\right)d\right]$ for *kh*=6.1~6.2, whereas the difference turns very small at *kh* = 5.5~5.7, meaning more close to resonance conditions. The bimodal frequency response of $\eta_{\max}^{(\mathrm{PTO})}$ for a large roof aperture might well be beneficial for situations with bimodal wave spectra, e.g., when wind seas and swell coexist. For $\bar{c}_{\mathrm{r}}$ ≥10, the peak and valley of the $\bar{c}_{\mathrm{opt}}^{(\mathrm{PTO})}$ -*kh* curves occur at *kh* = 6.2 and 8.2, respectively.

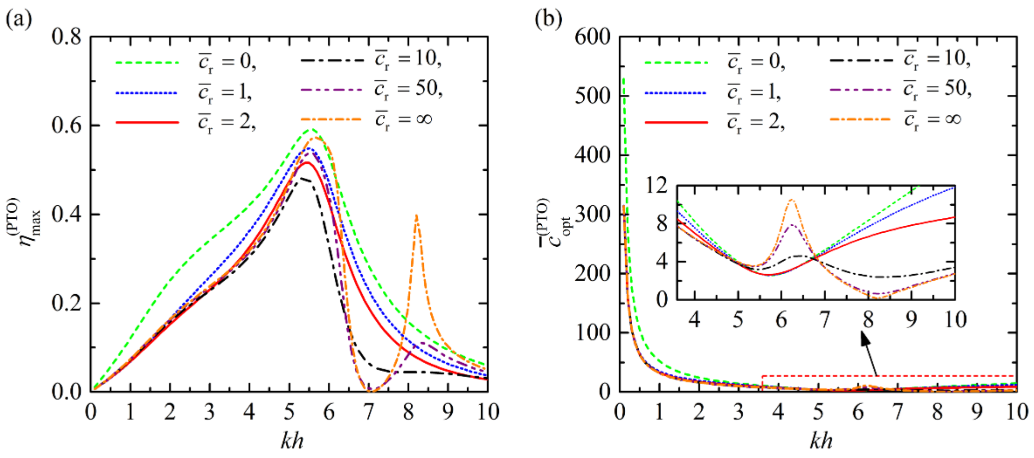

Fig. 14. Variation of $\eta_{\max}^{(\mathrm{PTO})}$ and $\bar{c}_{\mathrm{opt}}^{(\mathrm{PTO})}$ with *kh* for different $\bar{c}_{\mathrm{r}}$ and $\bar{k}_{\mathrm{m}}$=0.

4.2 Optimization of the mooring stiffness

When only the stiffness of the mooring lines can be changed, the maximum power capture factor $\eta_{\max}^{(\mathrm{m})}$ and $\overline{k}_{\mathrm{opt}}^{(\mathrm{m})}$ for $\overline{c}_{\mathrm{PTO}}$ =5 versus kh are illustrated in Fig. 15, in which different curves represent the device with different sizes of roof aperture. For small kh, i.e., kh < 5.0, the mooring stiffness is detrimental to power extraction, hence $\overline{k}_{\mathrm{opt}}^{(\mathrm{m})}$ = 0 is adopted. Whereas for large kh, i.e., kh > 6.0 for $\overline{c}_{\mathrm{r}}$ <2, the right value of $\overline{k}_{\mathrm{opt}}^{(\mathrm{m})}$ is beneficial for power absorption. The larger the value of kh, the larger the value of $\overline{k}_{\mathrm{opt}}^{(\mathrm{m})}$. Conversely, the smaller the value of $\overline{c}_{\mathrm{r}}$, the larger the value of $\overline{k}_{\mathrm{opt}}^{(\mathrm{m})}$. The comparison between Fig. 15a and Fig. 13 shows that the power absorption of the device can be significantly improved in short waves by properly increasing mooring stiffness.

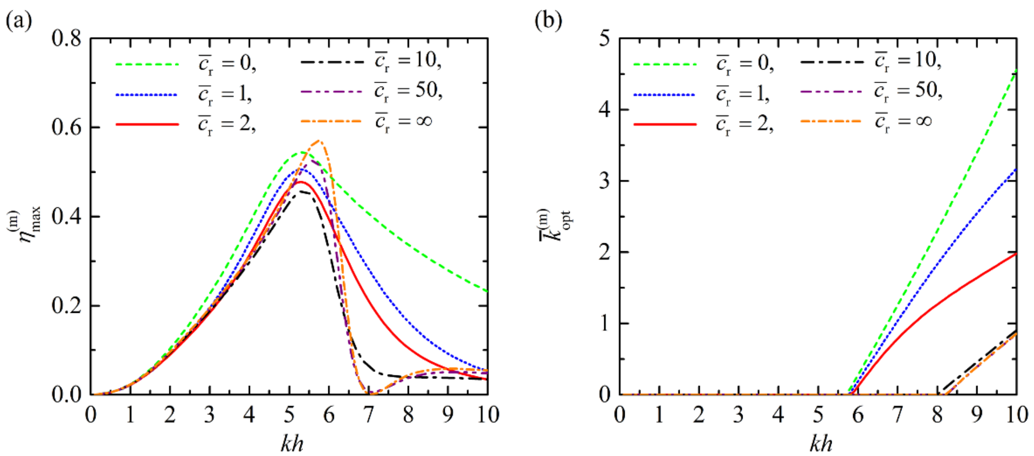

Fig. 15. Variation of $\eta_{\max}^{(\mathrm{m})}$ and $\overline{k}_{\mathrm{opt}}^{(\mathrm{m})}$ with kh for different values of $\overline{c}_{\mathrm{r}}$ ($\overline{c}_{\mathrm{PTO}}$=5).

4.3 Optimization of the roof damping coefficient

Figure 16 shows the variation of $\eta_{\max}^{(\mathrm{r})}$ and $\overline{c}_{\mathrm{opt}}^{(\mathrm{r})}$ with kh for different values of $\overline{c}_{\mathrm{PTO}}$ and $\overline{k}_{\mathrm{m}}$ = 0. Different curves represent the device with different PTO damping coefficients. As shown in Fig.16b, the optimal damping induced by a roof aperture $\overline{c}_{\mathrm{opt}}^{(\mathrm{r})}$ for maximizing power absorption of the novel WEC is either 0 or ∞. For kh < 5.0, the device with the roof aperture completely closed is preferred regardless of the value of PTO damping coefficient. Instead, for kh > 5.0 the device with the roof aperture totally open may capture more power depending on the value of the PTO damping, e.g., for 5.3 < kh < 6.3 for $\overline{c}_{\mathrm{PTO}}$=10, where an obvious bulge of the $\eta_{\max}^{(\mathrm{r})}$ -kh curve can be observed. As $\overline{c}_{\mathrm{PTO}}$ increases from 1 to 10, the main peak of

$\eta^{(r)}_{max}$-kh moves towards a smaller kh, and the peak value of $\eta^{(r)}_{max}$ first increases and then, after reaching 0.59 at kh = 5.5 for $\bar{c}_{PTO}$ = 3.0, decreases. Meanwhile, the bandwidth increases.

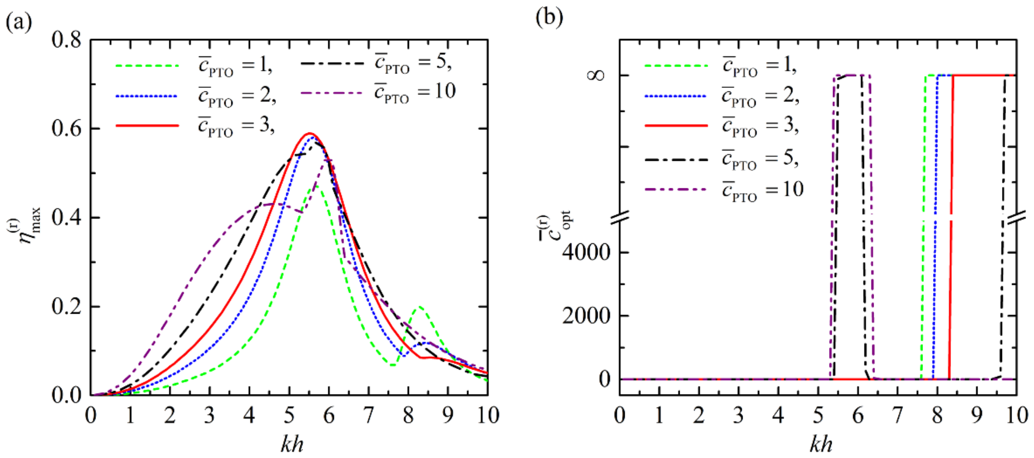

Fig. 16. Variation of $\eta^{(r)}_{max}$ and $\bar{c}^{(r)}_{opt}$ with kh for different $\bar{c}_{PTO}$ and $\bar{k}_m$=0.

When the novel WEC is subjected to extreme waves, it may be required to restrict its heave motion for the sake of survivability. For the VAPA WEC, the air pressure within the cylinder can be modified by adjusting the roof aperture. This may be used to minimize the heave motion, which naturally reduces power capture. The contrary of Fig. 16, Fig. 17 presents the results of $\eta^{(r)}_{min}$ and $\bar{c}^{(r)}_{min}$ when the power absorption of the device is minimized with a proper value of c_r. Comparing the two figures it is apparent that $\eta^{(r)}_{min}$ is much smaller than $\eta^{(r)}_{max}$. For example, the values of $\eta^{(r)}_{max}$ at kh = 5.5 are 0.46, 0.58, 0.59, 0.55 and 0.44, respectively, for $\bar{c}_{PTO}$=1, 2, 3, 5 and 10; whereas the values of $\eta^{(r)}_{min}$ are merely 0.34, 0.45, 0.47, 0.44 and 0.32, leading to a reduction in heaving amplitude of 13.9%, 11.7%, 10.6%, 10.8% and 14.0%, respectively. Under longer waves, e.g., kh=4.0, for $\bar{c}_{PTO}$=1, 2, 3, 5 and 10, a proper selection of the aperture size of the roof might result in the maximum reduction in heaving amplitude of 6.2%, 7.7%, 9.3%, 12.4% and 17.6%, respectively.

Another important aspect with reference to extreme waves is that viscous effects become relevant; under such conditions the linear model may overpredict the motion and power absorption of the WEC.

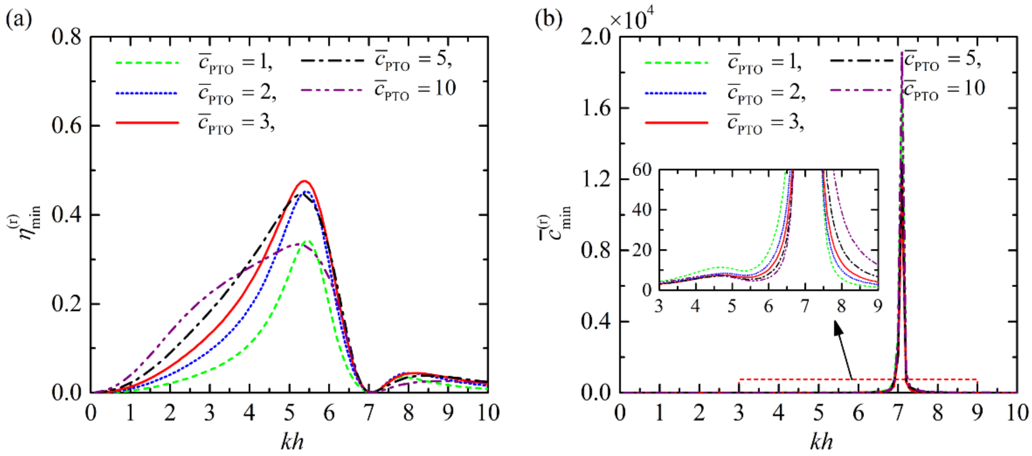

Fig. 17. Variation of $\eta_{\min}^{(\mathrm{r})}$ and $\bar{c}_{\min}^{(\mathrm{r})}$ with kh for different $\bar{c}_{\mathrm{PTO}}$ and $\bar{k}_{\mathrm{m}}=0$.

4.4 Optimization of the PTO damping coefficient and the roof damping coefficient

Results of $\eta_{\max}^{(\mathrm{PTO,r})}$ when c_{PTO} and c_{r} can be optimized simultaneously, and the corresponding $\bar{c}_{\mathrm{opt,PTO}}^{(\mathrm{PTO,r})}$ and $\bar{c}_{\mathrm{opt,r}}^{(\mathrm{PTO,r})}$ versus kh are shown in Fig. 18, in which different curves represent the device adopting different mooring stiffness. As $\bar{k}_{\mathrm{m}}$ increases from 0 to 2.0, the peak of $\eta_{\max}^{(\mathrm{PTO,r})}$ moves towards high wave frequencies with the peak value turning smaller and smaller. The maximum value of $\eta_{\max}^{(\mathrm{PTO,r})}$ is no more than $1/(2kR)$, which is the ratio of analytical maximum power capture width by a vertical asymmetrical heaving buoy relative to $2R$. For large mooring stiffness, e.g., $\bar{k}_{\mathrm{m}}=1.0$, 1.5 and 2.0, a bulge occurs at $5.5<kh<6.2$, where the corresponding $\bar{c}_{\mathrm{opt,r}}^{(\mathrm{PTO,r})}=\infty$. The sharp peak of the bulge occurs at $kh=6.0$ exactly, where the peak of $\bar{a}_{2,2}$ happens as shown in Fig.12c.

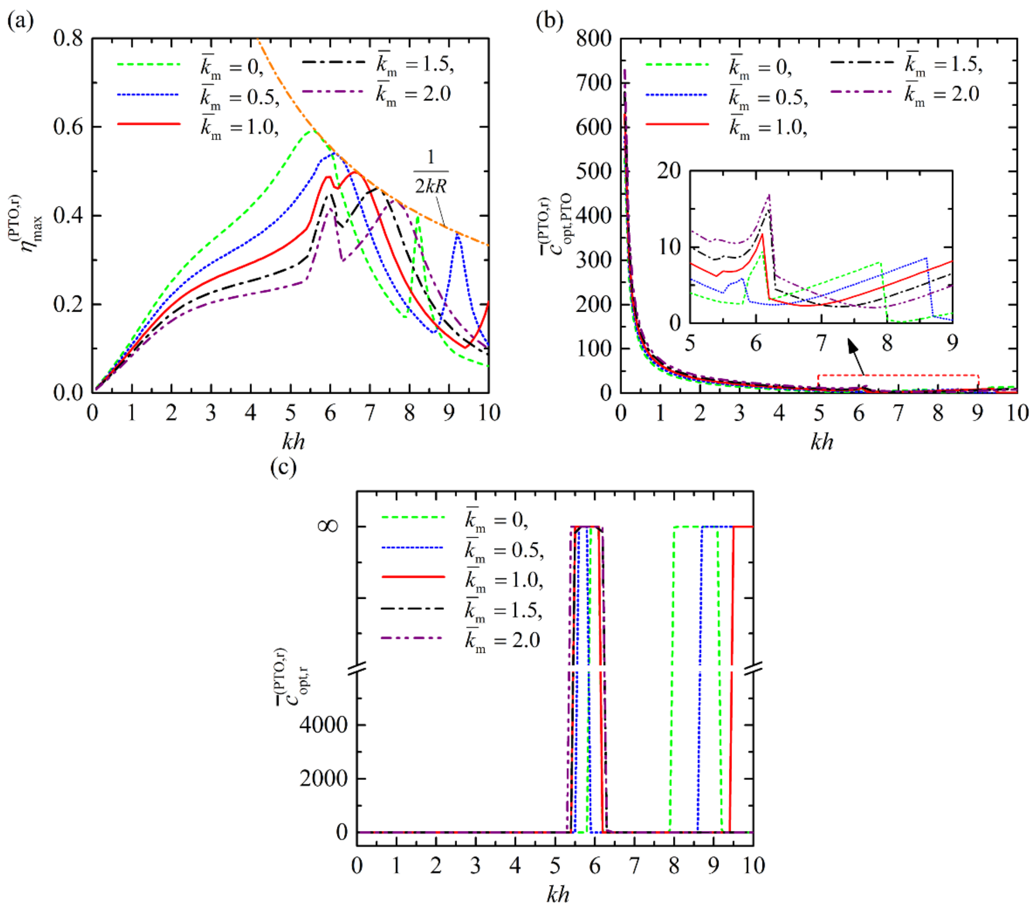

Fig. 18. Variation of $\eta_{\max}^{(\mathrm{PTO,r})}$, $\bar{c}_{\mathrm{opt,PTO}}^{(\mathrm{PTO,r})}$ and $\bar{c}_{\mathrm{opt,r}}^{(\mathrm{PTO,r})}$ with *kh* for different $\bar{k}_{\mathrm{m}}$.

4.5 Optimization of the PTO damping coefficient and the mooring stiffness

Results of $\eta_{\max}^{(\mathrm{PTO,m})}$ when c_{PTO} and k_{m} can be optimized simultaneously, and the corresponding $\bar{c}_{\mathrm{opt}}^{(\mathrm{PTO,m})}$ and $\bar{k}_{\mathrm{opt}}^{(\mathrm{PTO,m})}$ versus *kh* are shown in Fig. 19, in which different curves represent the device with different sizes of aperture on the roof. The device with the roof completely closed, i.e., $\bar{c}_{\mathrm{r}} = 0$, performs better in power extraction for the entire range of wave conditions studied. Note that for *kh* > 8.2, $\eta_{\max}^{(\mathrm{PTO,m})}$-*kh* with $\bar{c}_{\mathrm{r}} = \infty$ almost overlaps that for $\bar{c}_{\mathrm{r}} = 0$, while the device with the roof partly open presents a much smaller power capture capability. Even though both $\bar{c}_{\mathrm{r}} = 0$ and ∞ result in the same $\eta_{\max}^{(\mathrm{PTO,m})}$ for *kh* > 8.2, the $\bar{c}_{\mathrm{opt}}^{(\mathrm{PTO,m})}$ corresponding to $\bar{c}_{\mathrm{r}} = 0$ is much larger than that for $\bar{c}_{\mathrm{r}} = \infty$ (Fig.19b), e.g., $\bar{c}_{\mathrm{opt}}^{(\mathrm{PTO,m})}$ =1.69 and 0.21 at *kh*=9.0 for $\bar{c}_{\mathrm{r}}$ =0 and ∞, respectively. Consequently, the heaving amplitude for $\overline{c}_{\mathrm{r}}$ =∞ is 2.8 times as large as that for $\overline{c}_{\mathrm{r}}$ =0, implying that to achieve the same power absorption a much larger heave motion is required for the device with the roof completely open compared to that with the roof entirely closed. Given that the optimal mooring stiffness is independent of c_{PTO}, as derived in Eqs. (35) and (50) , the values of $\overline{k}_{\mathrm{opt}}^{(\mathrm{PTO,m})}$ (Fig.19c) are found to be similar to those of $\overline{k}_{\mathrm{opt}}^{(\mathrm{m})}$ (Fig.15b).

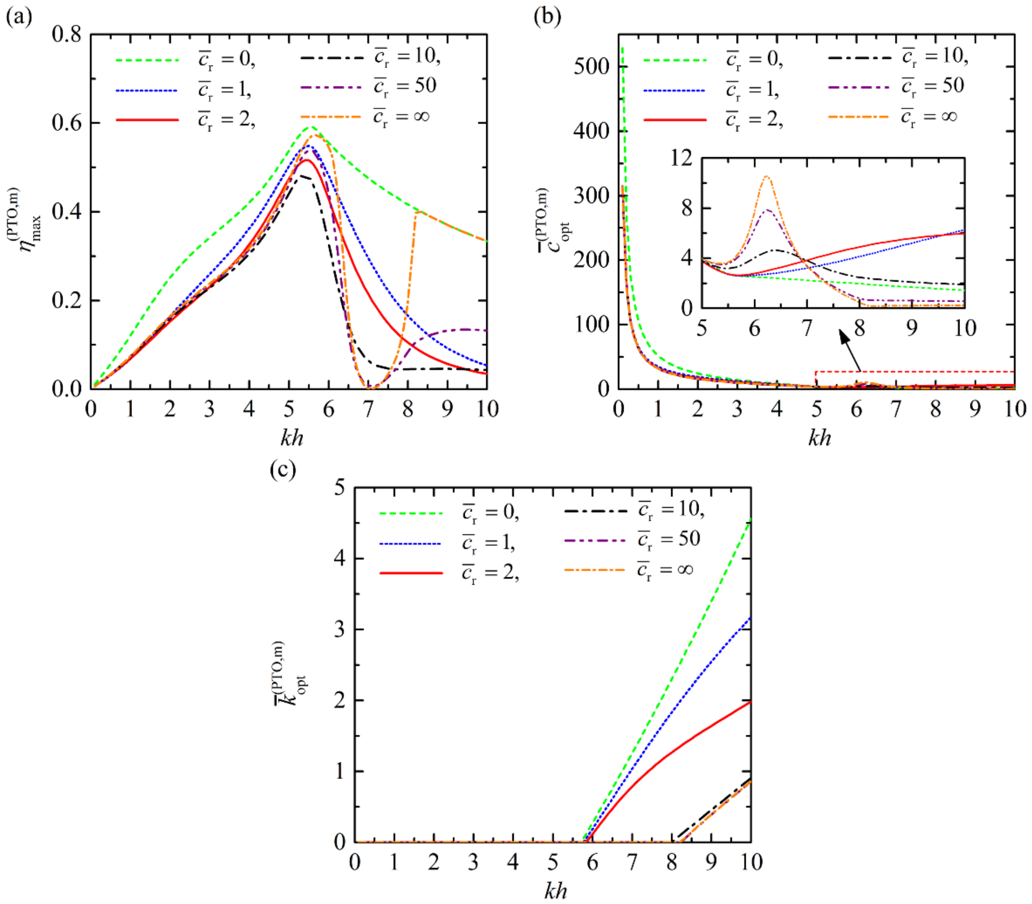

Fig. 19. Variation of $\eta_{\max}^{(\mathrm{PTO,m})}$, $\overline{c}_{\mathrm{opt}}^{(\mathrm{PTO,m})}$ and $\overline{k}_{\mathrm{opt}}^{(\mathrm{PTO,m})}$ with *kh* for different $\overline{c}_{\mathrm{r}}$.

4.6 Optimization of the roof damping coefficient and the mooring stiffness

Figure 20 presents the optimization results when c_{r} and k_{m} can be adjusted simultaneously, in which different curves represent the device for different values of c_{PTO}. When the PTO damping coefficient is large enough, e.g., $\overline{c}_{\mathrm{PTO}} \geq 5$, the device without any roof covering has a better performance in power extraction for certain wave conditions, e.g., $5.4 < kh < 6.2$ (Fig. 20b). Notwithstanding, for generic (unconstrained) wave conditions the device with the roof entirely closed is preferable. Thanks to the positive mooring stiffness for $kh > 6.0$ (Fig. 20c), the maximum power capture factor of the device can be increased significantly, which is apparent when comparing Figs. 20a and 16a. For $kh < 4.0$, the device with a larger value of $\bar{c}_{\mathrm{PTO}}$ can capture more power from waves; however, for wave conditions with large frequencies such that kh > 6.5, a large value of $\bar{c}_{\mathrm{PTO}}$ might be detrimental to power absorption. Indeed, for kh > 6.5, $\eta_{\max}^{(\mathrm{r,m})}$ with $\bar{c}_{\mathrm{PTO}}$=10 is much smaller than in all the other cases with smaller values of $\bar{c}_{\mathrm{PTO}}$ (Fig. 20a). Since the optimal mooring stiffness is independent of c_{PTO}, but does depend on c_{r}, the $\bar{k}_{\mathrm{opt}}^{(\mathrm{r,m})}$ -kh curves (Fig. 20c) overlap each other when the same value of $\bar{c}_{\mathrm{opt}}^{(\mathrm{r,m})}$ is adopted, regardless of the value of $\bar{c}_{\mathrm{PTO}}$.

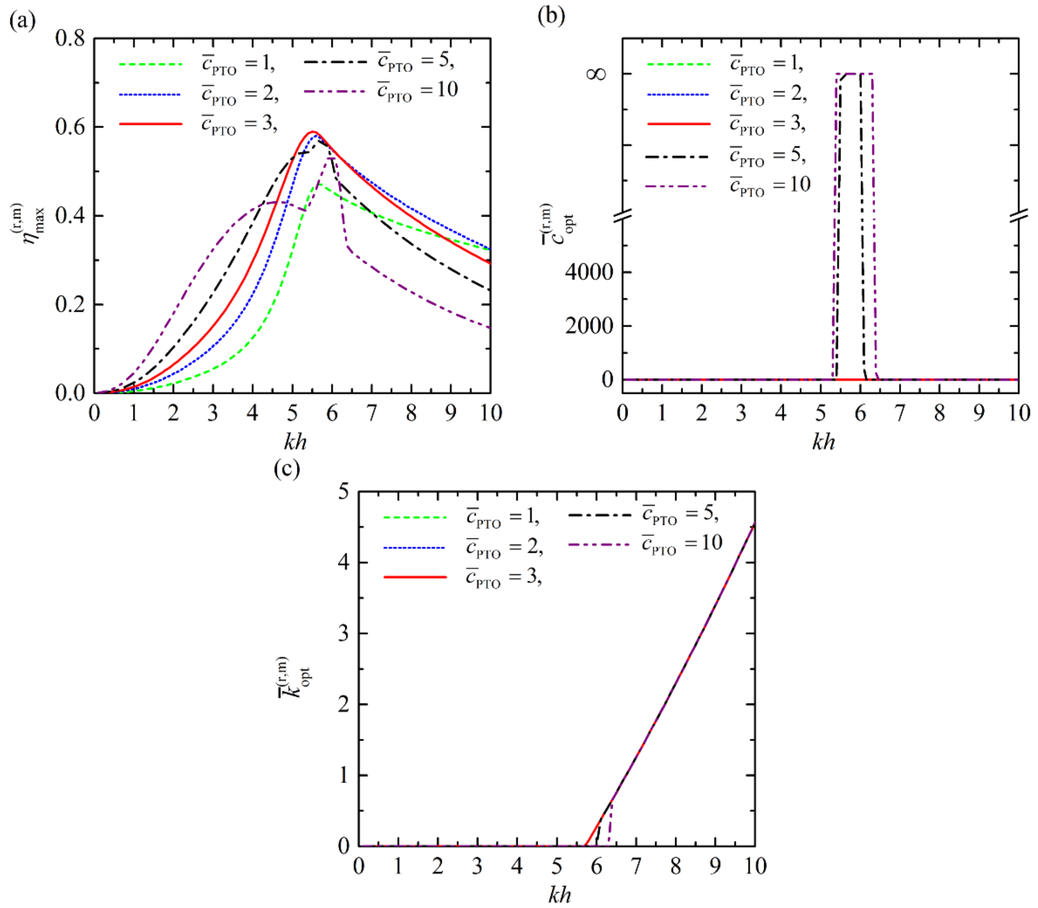

Fig. 20. Variation of $\eta_{\max}^{(\mathrm{r,m})}$, $\bar{c}_{\mathrm{opt}}^{(\mathrm{r,m})}$ and $\bar{k}_{\mathrm{opt}}^{(\mathrm{r,m})}$ with kh for different $\bar{c}_{\mathrm{PTO}}$.

4.7 Optimization of the PTO damping coefficient, the roof damping coefficient and the mooring stiffness

Figure 21 presents the frequency response of the maximum power capture factor when c_{PTO}, c_{r} and k_{m} are all optimized simultaneously. For kh > 5.7, $\eta_{\max}^{(\mathrm{PTO,r,m})}$ is equal to $1/(2kR)$.

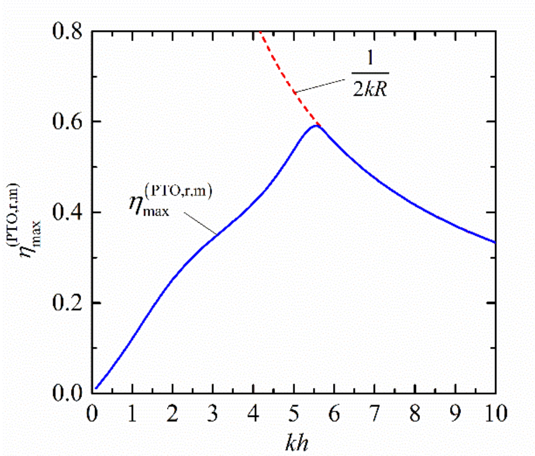

Fig. 21. Variation of $\eta_{\max}^{(\mathrm{PTO,r,m})}$ with kh.

5. Conclusions

In this paper a novel WEC, Variable Aperture Point-Absorber (VAPA), was proposed; it consists of a hollow cylinder capped by a roof with an aperture of variable size. To extract wave power the cylinder is connected by a tether to a linear generator on the seabed. The characteristics of power absorption of the WEC can be modified by adjusting the aperture on the roof. To study the performance of VAPA, the wave diffraction and radiation problems are solved with an analytical model. The influence of the PTO system and the roof aperture is represented by linear damping coefficients.

The power absorption of the novel WEC was found to be strongly dependent on three parameters: the PTO damping coefficient, the roof aperture damping coefficient and the non-negative mooring stiffness. A systematic analytical derivation of the maximum absorbed power was carried out under different optimization principles revolving around these three parameters. The following conclusions may be drawn.

First, changing the roof aperture modifies the frequency response of the wave capture factor.

Second, for unspecified wave conditions, the device generally captures more wave power with the roof aperture completely closed than with it completely open. Furthermore, with the roof aperture completely closed, the novel WEC performs similarly to a conventional (solid cylinder) point-absorber in terms of power capture. The VAPA WEC has, however, two significant advantages, a lower cost and enhanced survivability, thanks to its smaller displacement and lower surge motions.

Third, opening the roof aperture leads to a narrower bandwidth and a larger peak value of power capture relative to the configuration with the roof aperture closed. This may be advantageous when the wave conditions match the peak of the response of the device.

Fourth, if the configuration of the PTO is such that its damping can be tuned to the wave conditions, then increasing the size of the roof aperture leads gradually to a bimodal response, with the second peak (at kh = 8.3) corresponding to resonant conditions. This configuration would be ideal for bimodal sea states, when a swell and a wind sea coexist.

Fifth, the optimal mooring stiffness for the novel WEC was found to be independent of the PTO damping coefficient.

Finally, the Variable Aperture Point-Absorber, VAPA, presents the best power absorption when the roof aperture is completely open or entirely closed for any specified wave conditions. Intermediate values of the roof aperture are preferable, however, in storm conditions, for the adequate aperture was found to minimize power extraction and heave motions – an advantage for survivability.

In sum, a novel WEC concept, Variable Aperture Point-Absorber (VAPA), was presented and investigated by means of an *ad hoc* analytical model. A thorough analysis was carried out to determine its performance and optimize the values of PTO damping, roof aperture damping and mooring stiffness for power capture. Unlike conventional point-absorbers, VAPA is capable of minimizing heave motions, hence forces on the mooring lines, under extreme wave conditions. This is a significant advantage in that it can be the difference between surviving a storm or not.

The wave power absorption of the VAPA WEC proposed in this work might be further enhanced to some extent by capturing the surge or pitch motion for power generation. However, this must be balanced with the greater cost and, possibly, smaller robustness under extreme sea states of the more complicated PTO system that would be required – which will be considered in future work.

Acknowledgements

The research was supported by China Postdoctoral Science Foundation (Grant No. 2016M601041, 2017T100085), National Natural Science Foundation of China (51679124, 51479092) and Intelligent Community Energy (ICE), INTERREG V FCE, European Commission (Contract No. 5025).

Appendix A. Proofs of κ_1>0; ξ_3>0; $P_2 \equiv P_1$

κ_1>0 can be proved as follows, in which Eqs.(21)~(23) are adopted to express $a_{0,2}$ by $c_{0,0}$ and $c_{2,2}$:

$$
\begin{aligned}
\kappa_1 &= c_{2,2} + \mathrm{real}\left[S_{1,2}^2 \Big/ \left[c_{0,0} + c_\mathrm{r} - \mathrm{i}\omega\left(a_{0,0} + \frac{V_0}{c_a^2 \rho_0} \right) \right] \right] \\
&= c_{2,2} + \mathrm{real}\left[\frac{\left(c_{0,2} + \pi R_\mathrm{i}^2 \right)^2 - c_{0,0}c_{2,2} - 2\mathrm{i}\omega a_{0,2}\left(c_{0,2} + \pi R_\mathrm{i}^2 \right)}{c_{0,0} + c_\mathrm{r} - \mathrm{i}\omega\left(a_{0,0} + \frac{V_0}{c_a^2 \rho_0} \right)} \right] \\
&= c_{2,2} + \frac{\left[\left(c_{0,2} + \pi R_\mathrm{i}^2 \right)^2 - c_{0,0}c_{2,2} \right]\left(c_{0,0} + c_\mathrm{r} \right) - 2\omega^2 a_{0,2}\left(c_{0,2} + \pi R_\mathrm{i}^2 \right)\left(a_{0,0} + \frac{V_0}{c_a^2 \rho_0} \right)}{\left(c_{0,0} + c_\mathrm{r} \right)^2 + \omega^2\left(a_{0,0} + \frac{V_0}{c_a^2 \rho_0} \right)^2} \\
&= \frac{\left(c_r + c_{0,0} \right) c_\mathrm{r} c_{2,2} + \left(c_{0,2} + \pi R_\mathrm{i}^2 \right)^2 c_\mathrm{r} + \left[\left(c_{0,2} + \pi R_\mathrm{i}^2 \right)\sqrt{c_{0,0}} - sign\left(a_{0,2} \right)\sqrt{c_{2,2}}\,\omega\left(a_{0,0} + \frac{V_0}{c_a^2 \rho_0} \right) \right]^2}{\left(c_{0,0} + c_\mathrm{r} \right)^2 + \omega^2\left(a_{0,0} + \frac{V_0}{c_a^2 \rho_0} \right)^2} \\
&> 0
\end{aligned}
\quad . \tag{A1}
$$

In a similar way, $\xi_3>0$ is proved below,

$$
\begin{aligned}
\xi_3 &= c_{0,0} + \mathrm{real}\left[S_{1,2}^2 \Big/ \left(c_\mathrm{PTO} + \mathrm{i}\, k_\mathrm{m}/\omega + S_{2,2} \right) \right] \\
&= c_{0,0} + \mathrm{real}\left[\frac{\left(c_{0,2} + \pi R_\mathrm{i}^2 \right)^2 - c_{0,0}c_{2,2} - 2\mathrm{i}\omega a_{0,2}\left(c_{0,2} + \pi R_\mathrm{i}^2 \right)}{c_\mathrm{PTO} + c_{2,2} - \mathrm{i}\omega\left(a_{2,2} + m_0 - \frac{\rho g s_0 + k_\mathrm{m}}{\omega^2} \right)} \right] \\
&= c_{0,0} + \frac{\left[\left(c_{0,2} + \pi R_\mathrm{i}^2 \right)^2 - c_{0,0}c_{2,2} \right]\left(c_\mathrm{PTO} + c_{2,2} \right) - 2\omega^2 a_{0,2}\left(c_{0,2} + \pi R_\mathrm{i}^2 \right)\left(a_{2,2} + m_0 - \frac{\rho g s_0 + k_\mathrm{m}}{\omega^2} \right)}{\left(c_\mathrm{PTO} + c_{2,2} \right)^2 + \omega^2\left(a_{2,2} + m_0 - \frac{\rho g s_0 + k_\mathrm{m}}{\omega^2} \right)^2} \\
&= \frac{\left[\left(c_{0,2} + \pi R_\mathrm{i}^2 \right)^2 + c_{0,0}c_\mathrm{PTO} + c_{0,0}c_{2,2} \right] c_\mathrm{PTO} + \left[\left(c_{0,2} + \pi R_\mathrm{i}^2 \right)\sqrt{c_{2,2}} - sign\left(a_{0,2} \right)\sqrt{c_{0,0}}\,\omega\left(a_{2,2} + m_0 - \frac{\rho g s_0 + k_\mathrm{m}}{\omega^2} \right) \right]^2}{\left(c_\mathrm{PTO} + c_{2,2} \right)^2 + \omega^2\left(a_{2,2} + m_0 - \frac{\rho g s_0 + k_\mathrm{m}}{\omega^2} \right)^2} \\
&> 0
\end{aligned}
\quad . \tag{A2}
$$

$P_2 \equiv P_1$ is proved in Eq. (A3),

$$
\begin{aligned}
P_2 &= \frac{\left|F_{\mathrm{e}}^{(2)}\right|^2}{8c_{2,2}} \frac{\left|1-\dfrac{F_{\mathrm{e}}^{(0)}}{F_{\mathrm{e}}^{(2)}}\dfrac{S_{2,1}}{S_{1,1}}\right|^2}{\left\{1+\dfrac{1}{c_{2,2}}\mathrm{real}\left[S_{1,2}^2\Big/\left[c_{0,0}-\mathrm{i}\omega\left(a_{0,0}+\dfrac{V_0}{c_a^2\rho_0}\right)\right]\right]\right\}} \\
&= \frac{\left|F_{\mathrm{e}}^{(2)}\right|^2}{8c_{2,2}} \frac{\left|1+\mathrm{i}\sqrt{c_{0,0}/c_{2,2}}\,sign\left(a_{02}\right)\dfrac{c_{2,0}-\pi R_{\mathrm{i}}^2+\mathrm{i}\sqrt{c_{0,0}c_{2,2}}\,sign\left(a_{02}\right)}{c_{0,0}-\mathrm{i}\omega\left(a_{0,0}+\dfrac{V_0}{c_a^2\rho_0}\right)}\right|^2}{1+\dfrac{1}{c_{2,2}}\mathrm{real}\dfrac{\left(c_{2,0}-\pi R_{\mathrm{i}}^2\right)^2-c_{0,0}c_{2,2}+2\mathrm{i}\sqrt{c_{0,0}c_{2,2}}\,sign\left(a_{02}\right)\left(c_{2,0}-\pi R_{\mathrm{i}}^2\right)}{c_{0,0}-\mathrm{i}\omega\left(a_{0,0}+\dfrac{V_0}{c_a^2\rho_0}\right)}} \\
&= \frac{\left|F_{\mathrm{e}}^{(2)}\right|^2}{8c_{2,2}} \frac{\left[\sqrt{c_{0,0}}\left(c_{2,0}-\pi R_{\mathrm{i}}^2\right)sign\left(a_{02}\right)+\sqrt{c_{2,2}}\,\omega\left(a_{0,0}+\dfrac{V_0}{c_a^2\rho_0}\right)\right]^2}{\left[c_{0,0}^2+c_{2,2}\omega^2\left(a_{0,0}+\dfrac{V_0}{c_a^2\rho_0}\right)^2\right]+\left(c_{2,0}-\pi R_{\mathrm{i}}^2\right)^2 c_{0,0}+2\sqrt{c_{0,0}c_{2,2}}\,sign\left(a_{02}\right)\left(c_{2,0}-\pi R_{\mathrm{i}}^2\right)\omega\left(a_{0,0}+\dfrac{V_0}{c_a^2\rho_0}\right)} \\
&= \frac{\left|F_{\mathrm{e}}^{(2)}\right|^2}{8c_{2,2}} \equiv P_1
\end{aligned}
$$

, (A3)

in which Eq.(42) is used to express $F_{\mathrm{e}}^{(0)}\big/F_{\mathrm{e}}^{(2)}$ in terms of $c_{0,0}$ and $c_{2,2}$.

References

Abanades, J, Greaves, D, Iglesias, G, 2015. Wave farm impact on beach modal state, Marine Geology, 361, pp. 126-135.

ANSYS AQWA, 2011. Release. vol. 14. ANSYS-Inc., Pennsylvania, USA.

Astariz, S., Iglesias, G., 2015. The economics of wave energy: A review. Renewable and Sustainable Energy Reviews. 45, 397-408.

Astariz, S, Iglesias, G, 2016. Output power smoothing and reduced downtime period by combined wind and wave energy farms, Energy, 97, 69-81.

Babarit, A., Hals, J., Muliawan, M.J., et al., 2012. Numerical benchmarking study of a selection of wave energy converters. Renewable Energy. 41, 44-63.

BOLT Sea Power. BOLT Lifesaver Technical Introduction. available at: www.boltseapower.com [Accessed 16th April, 2018]

Budal, K., Falnes, J., 1975. A resonant point-absorber of ocean-wave power. Nature. 256, 478-479.

Carballo, R, Sanchez, M, Ramos, V, Taveira-Pinto, F, Iglesias, G, 2014. A high resolution geospatial database for wave energy exploitation, Energy, 68, pp. 572-583.

Chen, W., Dolguntseva, I., Savin, A., et al., 2017. Numerical modelling of a point-absorbing

wave energy converter in irregular and extreme waves. Applied Ocean Research. 63, 90-105.
Contestabile, P., Di Lauro, E., Buccino, M., Vicinanza, D., 2016. Economic assessment of Overtopping BReakwater for Energy Conversion (OBREC): a case study in Western Australia, Sustainability, 9(51).
Ding, B., Cazzolato, B.S., Arjomandi, M., et al., 2016. Sea-state based maximum power point tracking damping control of a fully submerged oscillating buoy. Ocean Engineering. 126, 299-312.
Drew, B., Plummer. A.R., Sahinkaya, M.N., 2009. A review of wave energy converter technology. Proceedings of the Institution of Mechanical Engineers, Part A: Journal of Power and Energy. 223, 887-902.
Engström, J., Sjökvist, L., Göteman, M., et al., 2017. Buoy geometry and its influence on survivability for a point absorbing wave energy converter: Scale experiment and CFD simulations. In: Proc. of the Marine Energy Technology Symposium, Washington DC, USA.
Evans, D.V., 1976. A theory for wave-power absorption by oscillating bodies. Journal of Fluid Mechanics. 77, 1-25.
Falcão, A.F.de O., Sarmento, A.J.N.A., 1980. Wave generation by a periodic surface pressure and its application in wave-energy extraction. In: International Congress of Theoretical and Applied Mechanics, Toronto, Canada.
Falcão, A.F.de O., 2010. Wave energy utilization: A review of the technologies. Renewable and Sustainable Energy Reviews. 14(3), 899-918.
Falnes, J., 2002. Ocean Waves and Oscillating Systems: Linear Interaction Including Wave-energy Extraction. Cambridge University Press, Cambridge, UK.
Göteman, M., 2017. Wave energy parks with point-absorbers of different dimensions. Journal of Fluids and Structures. 74, 142-157.
Gravråkmo, H., 2014. Buoy geometry, size and hydrodynamics for power take off device for point-absorber linear wave energy converter. Ph.D. thesis, Acta Universitatis Upsaliensis.
Hai, L., Göteman, M., Leijon, M., 2016. A methodology of modelling a wave power system via an equivalent RLC circuit. IEEE Transactions on Sustainable Energy. 7(4), 1363-1370.
Lejerskog, E., Boström, C., Hai, L., et al., 2015. Experimental results on power absorption from a wave energy converter at the Lysekil wave energy research site. Renewable Energy. 77, 9-14.
Lopez, M, Veigas, M, Iglesias, G, 2015. On the wave energy resource of Peru. Energy Conversion and Management, 90, pp. 34-40.
Iglesias, G., Carballo, R., 2009. Wave energy potential along the Death Coast (Spain), Energy 34, pp. 1963-1975.
Martins-Rivas, H., Mei, C.C., 2009. Wave power extraction from an oscillating water column along a straight coast. Ocean Engineering. 36, 426-433.
Mavrakos, S. A, Konispoliatis, D. N., 2012. Hydrodynamics of a free floating vertical axisymmetric oscillating water column device. Journal of Applied Mathematics. 3:2603-2621.
Mekhiche, M., Edwards, K.A., 2014. Ocean power technologies PowerBuoy: system-level

design, development and validation methodology. In: Proceedings of the 2nd Marine Energy Technology Symposium, 1-9.

Nader, J.R., 2013. Interaction of ocean waves with oscillating water column wave energy convertors. University of Wollongong, Australia, PhD.

Newman, J.N., 1976. The interaction of stationary vessels with regular waves. In Proceedings of the 11th Symposium on Naval Hydrodynamics. 491-501. Mechanical Engineering Pub., London.

Ransley, E.J., Greaves, D.M., Raby, A., et al., 2017. RANS-VOF modelling of the Wavestar point-absorber. Renewable Energy. 109, 49-65.

Sarmento, A.J.N.A., Falcão, A.F.de O., 1985. Wave generation by an oscillating surface-pressure and its application in wave-energy extraction. Journal of Fluid Mechanics. 150, 467-485.

Sjökvist, L., Göteman, M., 2017. Peak forces on wave energy linear generators in Tsunami and extreme waves. Energies. 10, 1323; doi: 10.3390/en10091323.

Sjolte, J., 2014. Marine renewable energy conversion. Grid and off-grid modelling, design and operation. PhD thesis. Norwegian University of Science and Technology.

Sjolte, J., Sandvik, C.M., Tedeschi, E., 2013a. Exploring the potential for increased production from the wave energy converter Lifesaver by reactive control. Energies. 6(8), 3706-3733.

Sjolte, J., Tjensvoll, G., Molinas, M., 2013b. Power collection from wave energy farms. Applied Sciences. 3, 420-436.

Ulvin, J.B., Molinas, M, Sjolte, J., 2012. Analysis of the power extraction capability for the wave energy converter BOLT. Energy Procedia. 20, 156-169.

Veigas, M, Ramos, V, Iglesias, G, 2014. A wave farm for an island: detailed effects on the nearshore wave climate, Energy, 69, pp. 801-812.

Veigas, M, Iglesias, G, 2014. Potentials of a hybrid offshore farm for the island of Fuerteventura, Energy Conversion and Management, 86, pp. 300-308.

Zheng, S., Zhang Y., 2015. Wave diffraction from a truncated cylinder in front of a vertical wall. Ocean Engineering. 104, 329-343.

Zheng, S., Zhang, Y., 2016. Wave radiation from a truncated cylinder in front of a vertical wall. Ocean Engineering. 111, 602-614.

Zheng, S., Zhang, Y., 2018. Theoretical modelling of a new hybrid wave energy converter in regular waves. Renewable Energy. 128, 125-141.

Zheng, S., Zhang, Y., Iglesias, G., 2018. Wave-structure interaction in hybrid wave farms. Journal of Fluids and Structures, 83, 386-412.